energies

MDPI

Article

Polysulfone Hollow-Fiber Membranes for Post-Combustion CO_2 Capture: Fabrication, Process Modeling, and Experimental Validation of a Continuous Membrane Column

Kirill A. Smorodin [1], Artem A. Atlaskin [1,*], Sergey S. Kryuchkov [1], Maria E. Atlaskina [1], Nikita S. Tsivkovsky [1], Alexander A. Sysoev [1], Vyacheslav V. Zhmakin [1], Anton N. Petukhov [2], Sergey S. Suvorov [2], Andrey V. Vorotyntsev [2,3] and Ilya V. Vorotyntsev [1]

[1] SMART Polymeric Materials and Technologies Laboratory, Mendeleev University of Chemical Technology of Russia, 125047 Moscow, Russia; smorodin.k.a@muctr.ru (K.A.S.); kriuchkov.s.s@muctr.ru (S.S.K.); atlaskina.m.ev@muctr.ru (M.E.A.); tsivkovskii.n.s@muctr.ru (N.S.T.); sysoev.a.a@muctr.ru (A.A.S.); vyacheslav.zhmakin@gmail.com (V.V.Z.); ilyavorotyntsev@gmail.com (I.V.V.)

[2] Chemical Engineering Laboratory, National Research Lobachevsky State University of Nizhny Novgorod, 603022 Nizhny Novgorod, Russia; antopetukhov@gmail.com (A.N.P.); serge.suvorov@gmail.com (S.S.S.); an.vorotyntsev@gmail.com (A.V.V.)

[3] Faculty of Chemistry, Lomonosov Moscow State University, 119991 Moscow, Russia

* Correspondence: atlaskin.a.a@muctr.ru

Abstract

This work presents an integrated experimental and modeling study of post-combustion CO_2 capture using polysulfone hollow-fiber membranes in a three-module «Continuous Membrane Column» cascade. Polysulfone hollow fibers were fabricated by dry–wet spinning, defect-healed with silicone, and characterized using both single gases and a humid four-component flue-gas mixture containing $N_2/O_2/H_2O/CO_2$ = 73.0/4.4/11.0/11.6 mol.%. The selected membrane exhibited a mixed-gas CO_2 permeance of 117 GPU with CO_2/N_2 and O_2/N_2 selectivities of 21.3 and 4.1, respectively. These experimentally determined transport parameters were implemented directly in an Aspen Plus model of the cascade. Two complementary simulation cases were considered: a process-scale calculation used for membrane-area sensitivity analysis and a laboratory-scale calculation using the actual membrane areas and feed-flow range employed in the experiments. In contrast to our previous studies, which were limited to process simulation, the present work extends the «Continuous Membrane Column» concept to full experimental validation using independently fabricated hollow-fiber membranes and a humid multicomponent feed. Both simulation scales predicted essentially the same characteristic behavior, with increasing overall stage cut leading to higher CO_2 recovery, lower residual CO_2 concentration, and reduced product purity. At the upper part of the investigated stage-cut range, the experimental CO_2 recovery reached approximately 80–81%, compared with approximately 82–83% predicted by the laboratory-scale model; the residual CO_2 concentration decreased below 1 mol.% experimentally, compared with approximately 1.8–1.9 mol.% predicted, while the product CO_2 concentration was approximately 67–70 mol.% experimentally and approximately 68–70 mol.% in the simulation. The results demonstrate that the model correctly reproduces the principal purity–recovery trade-off and the relevant operating window, while the remaining quantitative deviations indicate the influence of non-ideal hydrodynamic and engineering effects not captured by the idealized membrane-module description.

Academic Editor: Feng Lin

Received: 2 October 2026
Revised: 5 November 2026
Accepted: 6 November 2026
Published: 7 November 2026

Copyright: © 2026 by the authors. Licensee MDPI, Basel, Switzerland. This article is an open access article distributed under the terms and conditions of the Creative Commons Attribution (CC BY) license.

Keywords: post-combustion CO_2 capture; hollow-fiber membranes; polysulfone; membrane cascade; Continuous Membrane Column; mixed-gas permeation; process simulation

1. Introduction

Carbon capture, utilization and storage (CCUS) is an important component of decarbonization strategies for stationary and energy-intensive emission sources. Post-combustion capture is particularly attractive for retrofit applications, but the low CO_2 concentration (typically 10–15 mol.%) and near-atmospheric pressure of flue gas make the separation intrinsically challenging [1–5]. Practical capture technologies must therefore combine separation efficiency with scalability, moderate energy demand, and compatibility with continuous operation [6–8].

Amine absorption remains the reference post-combustion technology but requires substantial regeneration energy and is affected by corrosion and solvent degradation [2,5,9]. Adsorption, cryogenic separation, and hybrid approaches likewise involve pressure, temperature, or regeneration constraints [8,10]. These limitations have stimulated strong interest in membrane-based CO_2 capture.

Membrane separation is attractive because it is continuous, modular, reagent-free, and does not require thermal sorbent regeneration [1,3,11]. Post-combustion operation nevertheless requires high CO_2 permeance and selectivity, stability in humid streams, mechanical integrity, and scalability [6,7,12]. Although many advanced membrane materials show high laboratory performance, their translation to large-area industrial modules remains challenging [4,12,13].

Process configuration is equally important because the low CO_2 partial pressure requires feed compression, permeate evacuation, or both. Excessive feed compression is energetically unfavorable, whereas deep vacuum increases equipment size and operating costs [14–16]. Consequently, multistage systems, recycle streams, sweep configurations, and moderate compression/vacuum combinations have been widely investigated [17–20], and membrane permeance, selectivity, area, pressure ratio, and stage cut must be considered jointly [15,21,22].

Merkel et al. demonstrated that highly permeable CO_2-selective membranes can become competitive when integrated into an appropriately designed post-combustion process [23]. The subsequently developed Polaris™ technology progressed to pilot-scale testing with actual power-plant flue gas [24,25], while other pilot studies using fixed-site-carrier and thin-film composite membranes similarly emphasized evaluation under realistic module-scale conditions [26–28].

A persistent limitation of membrane-process studies is the use of hypothetical transport properties or dense-film data obtained under conditions different from the target process [21,22,29]. Pure-gas permeability and ideal selectivity may not represent humid multicomponent module performance, where competitive sorption, aging, defects, pressure losses, concentration polarization, and non-ideal flow distribution can become important [14,30,31]. Experimental validation using transport characteristics measured under process-relevant conditions is therefore essential.

Hollow fibers are well suited to such validation because of their high membrane-area-to-volume ratio and compatibility with continuous manufacturing. Polysulfone (PSF) combines mechanical and thermal stability, commercial availability, and reliable phase-inversion processing, providing a technologically accessible platform for linking membrane fabrication with module and process performance [31,32].

Water vapor is particularly relevant because real flue gas contains substantial H_2O, which can affect polymer free volume, competitive sorption, gas permeance, and downstream compression. Accordingly, transport data obtained with dry pure gases cannot always be transferred directly to humid flue-gas separation [11,27,28].

Our previous studies introduced the "Continuous Membrane Column" cascade concept [33]. A binary CO_2/N_2 study showed that the cascade could theoretically achieve at least 95 mol.% CO_2 purity, 90% recovery, and residual CO_2 below 2 mol.% [34]. A subsequent study extended the model to a realistic wet four-component flue gas and compared alternative cascade configurations [35]. These simulations identified membrane selectivity and membrane area as key variables and established the most promising process configuration.

Those previous calculations employed transport parameters representative of high-performance MTR Polaris membranes and remained experimentally unverified. In the present work, the selected cascade configuration was therefore recalculated using experimentally fabricated PSF hollow-fiber membranes.

The principal novelty of the present study therefore lies not in achieving higher separation performance than in our previous simulation-based analyses, which employed high-performance membrane transport properties, but in the experimental validation of the previously simulation-only "Continuous Membrane Column" concept using independently fabricated PSF hollow-fiber modules and a humid four-component flue-gas mixture. In the practically relevant operating region ($\theta \approx 0.158$), the experimental and laboratory-scale simulated values differed by only approximately 1.1 percentage points for both CO_2 recovery and product CO_2 concentration, while the residual CO_2 concentration differed by approximately 0.7 percentage points. This quantitative agreement demonstrates that the model captures the principal cascade behavior under experimentally reproduced conditions, while the remaining deviations primarily reflect non-ideal module and hydrodynamic effects.

Representative membrane-process studies for post-combustion CO_2 capture are summarized in Table 1. The comparison intentionally includes predominantly simulation-based studies together with two pilot-scale experimental studies, so that process projections can be distinguished from experimentally demonstrated separation performance.

Table 1. Representative membrane-process studies for post-combustion CO_2 capture.

Study	Membrane Material	Feed Composition	Operating Conditions	Main Separation Result
Merkel et al. [23] Simulation-based	High-permeance CO_2-selective polymer membrane; $Q(CO_2) \approx 1000$ GPU, $\alpha(CO_2/N_2) \approx 50$	Wet flue gas: 11.6% CO_2, 11% H_2O, 4.2% O_2, balance N_2	600 MWe reference plant; two-step vacuum or counter-flow/sweep desogn; Pf ≈ 2 bar, Pp ≈ 0.2 bar	>95% CO_2 product; 90% CO_2 recovery
Zhao et al. [17] Simulation-based	Commercial polymer membrane; $Q(CO_2) \approx 185$ GPU, $\alpha(CO_2/N_2) \approx 43$	Simplified flue gas ≈13.5% CO_2 in N_2	Multi-stage cascade; second enrichment stage ≈ 4 bar; first-stage vacuum varied	95% CO_2 product; 90% CO_2 recovery
Ramasubramanian et al. [18] Simulation-based	Hypothetical membrane; $Q(CO_2) \approx 3000$ GPU, $\alpha(CO_2/N_2) \approx 140$	Coal flue gas, ≈13% CO_2 in N_2	Air-sweep two-stage process; Pf ≈ 1 bar; Pp ≈ 0.2 bar	95% CO_2 product; 90% CO_2 recovery
Atlaskin et al. [34] Simulation-based	Polaris-type membrane; $Q(CO_2) = 1000$ GPU, $\alpha(CO_2/N_2) = 50$	17% CO_2 in N_2	Continuous Membrane Column; 50 °C; Pf/Pp = 0.15/0.02 MPa	97.2 mol.% CO_2 product; >90% recovery; 1.87 mol.% residual CO_2

Smorodin et al. [35] Simulation-based	Polaris-type membrane; Q(CO_2) = 1000 GPU, α(CO_2/N_2) = 50	Wet flue gas: 11.6% CO_2, 11% H_2O, 4.4% O_2, balance N_2	Wet four-component Continuous Membrane Column and reference cascades; 50 °C; Pf/Pp = 0.15/0.02 MPa	≥95 mol.% CO_2 product; ≥90% recovery; ≤2 mol.% residual CO_2
White et al. [24] Experimental-based	Polaris spiral-wound modules	Real coal-derived and simulated natural-gas flue gas	1 ton CO_2 day−1 pilot; cross-flow and sweep modules; extended runs up to 1800 h	62.6% CO_2 product >90% CO_2 recovery 4.29% residual CO_2
Pohlmann et al. [26] Experimental-based	PolyActive thin-film composite membrane	Real wet coal flue gas: ≈14.5% CO_2, 6.5% O_2, 14% H_2O and trace impurities	Single-stage pilot; ≈80 °C; feed/permeate pressure and flow varied	≈50–75% CO_2 product; ≈42.7% CO_2 recovery

Overall, the literature remains dominated by simulation-based process studies, and many of these analyses employ binary CO_2/N_2 or otherwise simplified feed mixtures. Experimental validation with real or representative humid multicomponent flue gas is much less common. The present work addresses this gap by combining membrane fabrication and wet mixed-gas characterization with process simulation and direct experimental validation of the complete cascade.

Accordingly, this study integrates PSF hollow-fiber fabrication, single- and mixed-gas characterization, process simulation, and experimental validation of the complete "Continuous Membrane Column" cascade. Transport properties were measured under the relevant wet-gas conditions (50 °C; 150/20 kPa feed/permeate pressures), introduced directly into the mathematical model, and used for both membrane-area sensitivity analysis and direct comparison with the laboratory cascade.

2. Materials and Methods

2.1. Materials

Commercial polysulfone (PSF, Udel® P3500LCDMB7, Solvay, Brussels, Belgium) was used as the membrane-forming polymer. N,N-Dimethylformamide (DMF), tetrahydrofuran (THF), and isopropyl alcohol (IPA) were employed for preparation of the spinning dope. DMF acted as the principal polymer solvent, THF was introduced as a volatile co-solvent affecting the formation of the selective surface layer, while IPA was used as a non-solvent additive. The same polymer/solvent system was previously shown to be suitable for fabrication of asymmetric PSF hollow fibers.

Distilled water was used as the internal and external coagulation medium during hollow-fiber spinning and for subsequent washing of the as-spun fibers. Isopropanol and hexane were used during solvent-exchange post-treatment to minimize structural collapse during drying. A Sylgard silicone elastomer was additionally used as a defect-healing agent for post-treatment of selected hollow-fiber membranes prior to gas-permeation experiments.

High-purity nitrogen (≥99.999%), oxygen (≥99.995%), and carbon dioxide (≥99.95%), were used for determination of the membrane gas-transport characteristics and for preparation of the model flue-gas mixture, which contains 73.0/4.4/11.0/11.6 mol. % of nitrogen, oxygen, water vapors and carbon dioxide. Gas mixture of dry gases was prepared via standard manometric method and pressurized in gas cylinder under the pressure of 6 MPa, further, mixture was bubbled through the water at 51 °C (in case of cascade experiments). Distilled water was used as the source of water vapor. Helium was used as the carrier gas for gas-chromatographic analysis.

2.2. Spinning of Polysulfone Hollow-Fiber Membranes

Asymmetric polysulfone hollow fibers were fabricated by a dry–wet spinning process based on non-solvent-induced phase separation. The spinning solution contained PSF, DMF, THF, and IPA at a mass ratio of 28/50/15/7 wt.%, respectively. This composition was selected to provide sufficient polymer concentration for mechanical stability while maintaining a viscosity suitable for continuous hollow-fiber spinning. In this formulation, DMF ensured complete dissolution of PSF, whereas the more volatile THF promoted formation of the outer selective layer during passage of the nascent fiber through the air gap. IPA shifted the dope composition closer to the phase-separation boundary and therefore influenced the development of the porous support structure.

The hollow fiber membranes were prepared using pilot-industrial spinning line, the principal scheme of which is given in Figure 1. The spinning dope was prepared in a thermostated vessel. DMF was first heated to 50 °C, after which PSF was gradually introduced under continuous agitation. Incremental polymer addition was used to obtain a homogeneous solution and to avoid formation of agglomerates. After complete dissolution of the polymer, the solution was maintained under stirring at the same temperature, followed by sequential addition of THF and IPA. The resulting four-component solution was mixed until visually homogeneous and subsequently transferred to the spinning reservoir. Prior to spinning, the dope was left undisturbed for at least 15 h to allow entrained gas bubbles to be removed.

Hollow fibers were produced using a coaxial spinneret supplied independently with the polymer solution and the bore liquid. The dope was delivered through the annular channel, whereas distilled water was introduced through the central channel as the internal coagulant. The corresponding spinneret diameters were 0.50 mm for the polymer-solution outlet and 0.33 mm for the bore channel. Both the spinning dope and the bore fluid were maintained at 35 °C. The flow rates of the polymer solution were kept at 1.28 g min^{-1}, meanwhile internal coagulant flowrate was fixed at 1.1 g min^{-1}.

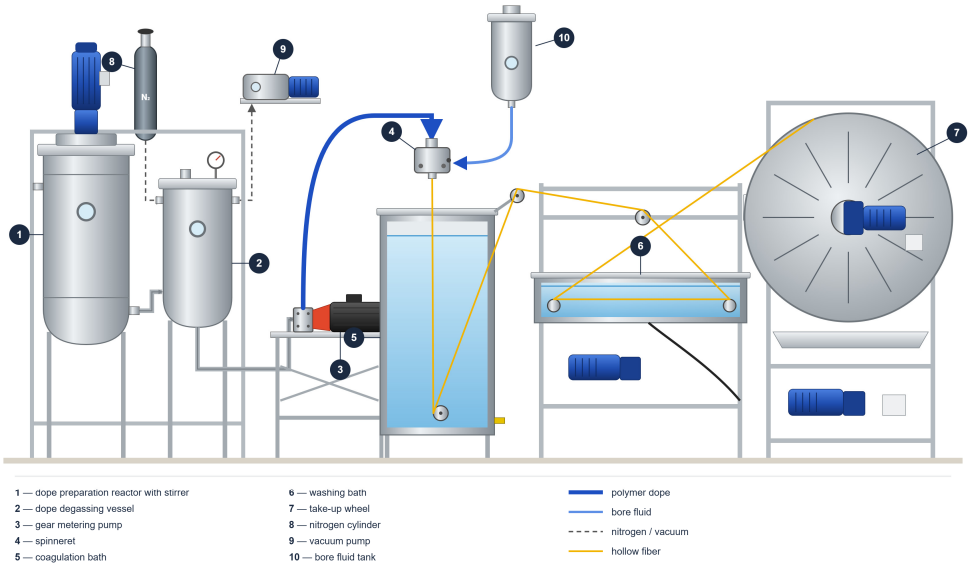


Figure 1. Hollow fiber membrane spinning line.

After leaving the spinneret, the nascent hollow fiber passed through an air gap before entering the external coagulation bath containing water at 25 °C. The take-up velocity was fixed at 17 m min^{-1}, whereas the nascent fiber exited the spinneret at an estimated linear velocity of approximately 14 m min^{-1}, corresponding to a draw ratio of approximately

1.22–1.25. Based on the take-up velocity, the estimated residence time of the nascent fiber in the air gap ranged from approximately 0.56 s at 16 cm to 0.92 s at 26 cm.

To obtain membrane batches with different skin-layer structures and, consequently, different gas-transport characteristics, the spinneret-to-coagulation-bath distance was varied between 16 and 26 cm in 2 cm increments. Thus, six batches of PSF hollow fibers were prepared under otherwise identical spinning conditions.

Following phase inversion, the fibers were thoroughly washed to remove residual solvent. A stepwise solvent-exchange procedure was then applied to preserve the porous substructure during drying. The fibers were first stored in water for 48 h, transferred to IPA for a further 48 h, and then immersed in hexane for 8 h. After solvent exchange, the fibers were dried under reduced pressure for 12 h at a residual pressure of approximately 10 kPa.

Because highly permeable asymmetric hollow fibers may contain a limited number of non-selective pinhole defects, a silicone post-treatment was additionally applied to the fibers selected for membrane-module fabrication. A thin Sylgard-based coating was deposited onto the external fiber surface to seal such defects without intentionally forming a thick independent gas-separation layer. The purpose of this treatment was therefore to restore the effective selectivity of the PSF selective skin while retaining the highest possible gas permeance.

2.3. Hollow-Fiber Post-Treatment and Module Preparation

The as-spun polysulfone hollow fibers were first characterized in their untreated state to determine their initial gas-transport properties. For these measurements, laboratory-scale membrane modules containing 50–100 hollow fibers were assembled. The fibers were arranged in parallel bundles and fixed at both ends using an epoxy potting compound, while the fiber lumens remained open for permeate withdrawal.

Following the solvent-exchange and drying procedure described above and the initial gas-permeation characterization, the assembled membrane modules were subjected to defect healing with Sylgard™ 184 Silicone Elastomer. A 5 wt.% solution of Sylgard™ 184 in n-heptane was introduced into each module from the shell side until the hollow-fiber bundle was completely filled and the external fiber surfaces were uniformly wetted. The filled module was then placed on a vibration platform for 8 h to promote homogeneous distribution of the coating solution throughout the fiber bundle and ensure uniform contact with the outer selective surface. After treatment, the remaining silicone solution was drained from the shell side, and the module was dried at 50 °C while a low continuous flow of dry nitrogen was passed through the fiber lumens. The silicone treatment was used exclusively as a defect-healing step to seal occasional non-selective surface pinholes and suppress bypass transport, rather than to form an additional independent selective layer.

After completion of the drying step, the Sylgard-treated modules were characterized under the same single-gas conditions as the untreated modules. Comparison of the permeance and selectivity values before and after post-treatment was used to evaluate the effectiveness of defect healing and to select the membrane batch for subsequent mixed-gas and cascade experiments.

2.4. Single-Gas Permeation Measurements

The single-gas transport properties of the prepared hollow-fiber membranes were determined using a simple volumetric method with a soap-film flowmeter (Figure 2). The membrane module (1/4″ stainless steel tube) was connected to a gas cylinder containing the test gas through a pressure regulator, and the gas was supplied to the shell side of the hollow fibers. Measurements were performed at feed pressures of 0.23 MPa, meanwhile permeate side pressure was 0.1 MPa. During each experiment, the permeate leaving the

fiber lumen was directed to the soap-film flowmeter, where the volumetric permeate flow rate was measured directly. The procedure was repeated separately for each test gas.

For the displacement volumes and measurement times used in the experiments, the combined relative uncertainty of the calculated single-gas permeance was approximately 3% and did not exceed 4%. For each spinning batch, three independently assembled membrane modules were tested, and the reported permeance and selectivity values represent the corresponding mean values. Considering propagation of the permeance uncertainties, the relative uncertainty of the calculated ideal selectivity did not exceed approximately 5.7%.

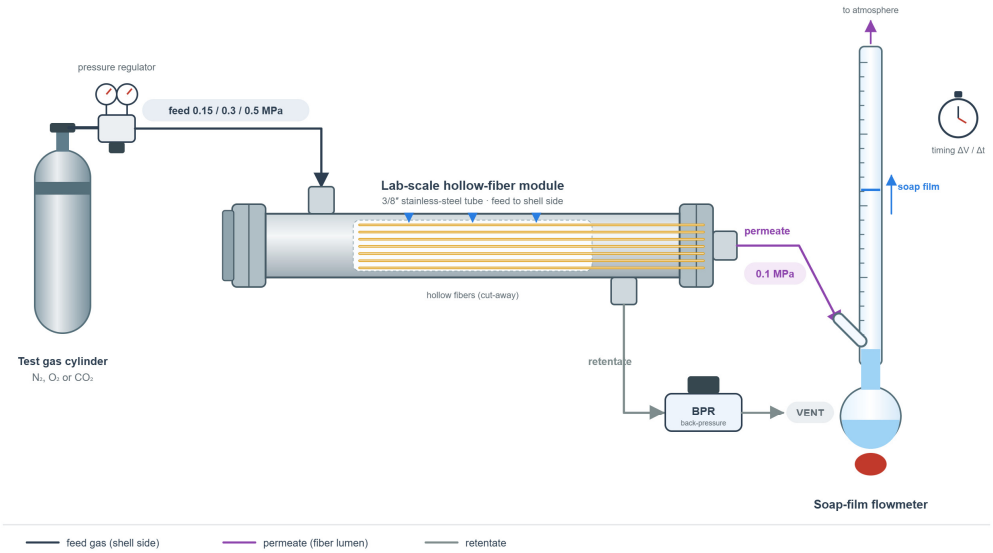


Figure 2. Principal scheme of the express test unit for single gas permeation test.

The gas permeance, Q_i, was calculated from the measured permeate flow rate according to:

$$Q_i = \frac{J_i}{A\Delta p_i}$$

where Q_i is the gas permeance of component i, J_i is the volumetric permeate flow rate of component $_i$, A is the effective membrane area, and Δp_i is the transmembrane partial-pressure difference in component i. For pure-gas measurements, Δp_i corresponds to the pressure difference in the tested gas across the membrane.

The ideal selectivity for a gas pair i/j was calculated as:

$$\alpha_{i/j} = \frac{Q_i}{Q_j}$$

where $\alpha_{i/j}$ is the ideal selectivity for gas pair i/j, while Q_i and Q_j are the corresponding single-gas permeances. This rapid screening procedure was used to compare the gas-transport characteristics of different hollow-fiber batches and to evaluate changes in membrane performance before and after the Sylgard™ 184 defect-healing treatment.

2.5. Mixed-Gas Permeation Measurements

After the preliminary single-gas screening, the selected hollow-fiber modules were characterized using a wet multicomponent gas representative of post-combustion flue gas. The target composition was $N_2/O_2/H_2O/CO_2$ = 73.0/4.4/11.0/11.6 mol.%. Unlike the single-gas tests, the four-component feed was generated continuously immediately upstream of the membrane test section rather than prepared in advance in a storage cylinder.

Throughout this work, unless explicitly stated otherwise, mixed-gas compositions are reported on a wet basis. Thus, the composition $N_2/O_2/H_2O/CO_2$ = 73.0/4.4/11.0/11.6 mol.% includes water vapor in the 100 mol.% total. After exclusion of H_2O and renormalization of the remaining components, the corresponding dry-basis composition is $N_2/O_2/CO_2$ = 82.02/4.94/13.03 mol.%. Accordingly, throughout Section 2.5 and in the subsequent discussion of mixed-gas permeation, the term "mixed gas" refers to the humid four-component mixture containing water vapor unless explicitly stated otherwise.

A schematic of the mixed-gas permeation setup is shown in Figure 3. The dry-gas section was equipped with FG-201 CV mass-flow controllers (Bronkhorst, Nuland, The Netherlands), which independently metered the CO_2 and O_2 streams. Water vapor was introduced using a controlled evaporation and mixing (CEM) system. Nitrogen served both as a major component of the model flue gas and as the carrier stream for the CEM unit. Distilled water was supplied to the evaporator at a controlled rate, completely vaporized, and mixed with the N_2 carrier gas. The humidified nitrogen stream was subsequently combined with the dry CO_2 and O_2 streams. The individual gas and liquid flow rates were selected to obtain the required final composition of 73.0 mol.% N_2, 4.4 mol.% O_2, 11.0 mol.% H_2O, and 11.6 mol.% CO_2. The total gas flow delivered by the mixing section could be varied up to approximately 750 cm^3 min^{-1}. All tubing located downstream of the CEM unit was thermostated at 50 °C to prevent condensation and preserve the set water-vapor content.

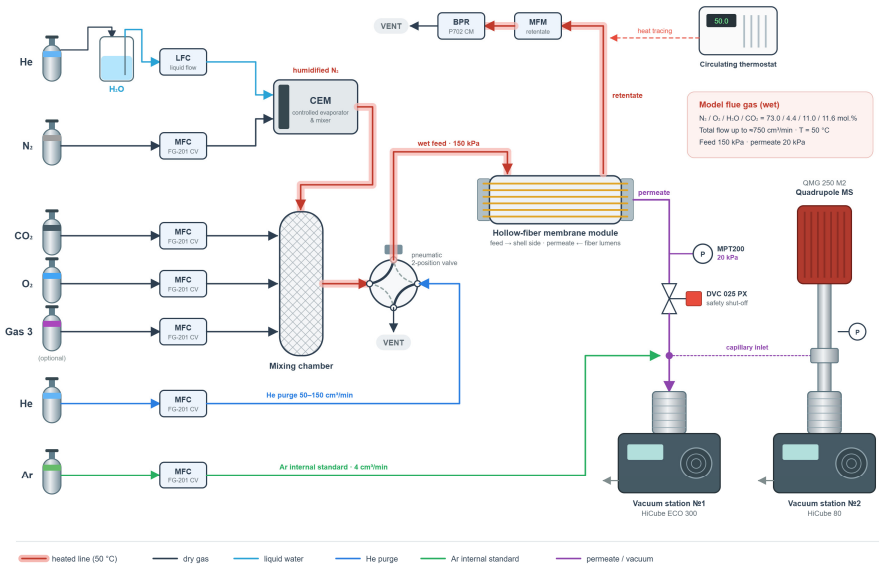


Figure 3. Mixed-gas permeation test unit coupled with mass spectrometer.

The resulting wet gas mixture was fed to the shell side of the hollow-fiber module. A P702 CM back-pressure regulator (Bronkhorst, Nuland, The Netherlands) installed in the retentate line maintained the feed-side pressure at 150 kPa. The permeate was withdrawn from the fiber lumens by a Hi-Cube ECO 300 pumping station (Pfeiffer Vacuum, Asslar, Germany), providing a permeate-side pressure of 20 kPa. This pressure was continuously monitored with an MPT200 pressure transmitter. A DVC 025 PX solenoid-operated diaphragm valve was placed between the module and the vacuum station and served as a safety shut-off element in the event of a sudden pressure rise caused, for example, by membrane or module failure.

The permeate composition was monitored online with a QMG 250 M2 quadrupole mass spectrometer (Pfeiffer Vacuum, Asslar, Germany). The analyzer was connected to a separate Hi-Cube 80 pumping station, which maintained the pressure required for mass-

spectrometric operation. Before each run, the membrane module and gas-distribution lines were flushed with helium at 50–150 $cm^3\ min^{-1}$ to remove residual air and gases remaining from the preceding experiment. After the purge stage, a pneumatically actuated two-position valve switched the module feed from the helium line to the freshly prepared wet gas mixture. In this configuration, the permeation response could be followed continuously from the moment the membrane contacted the model flue gas until steady-state transport was reached.

No intentional drying of the membrane was performed between humid mixed-gas experiments. Since the target post-combustion application involves continuous contact with water-containing flue gas, the membrane modules were evaluated under continuously humid operating conditions. Consequently, repeated humidification–drying cycling was outside the scope of the present study.

Operating variables were recorded continuously. FlowPlot V.3.35 software was used to log the gas flow rates and the pressure on the feed side of the membrane module, whereas PV MassSpec V.21.04.01-b and PV TurboViewer V.01.04.00 were used to acquire the mass spectra and monitor the low-pressure section. The mass-spectrometric signal was updated with a time resolution of 1 ms, enabling both transient and steady-state membrane responses to be recorded. Only the data obtained after stabilization of the feed flow rates, pressures, and component signals were used for calculation of the membrane transport parameters.

For quantitative determination of component fluxes, argon was introduced into the permeate analytical line as an internal standard at a constant flow rate of 4 $cm^3\ min^{-1}$. The calibrated mass-spectrometer response was converted into the partial pressure of each detected component. Since the argon flow was known, the volumetric permeate flow of component *i* was obtained from the ratio between the partial pressures of that component and the internal standard:

$$\frac{J_i}{J_{Ar}} = \frac{p_i}{p_{Ar}}$$

where J_i and J_{Ar} are the volumetric flow rates of component *i* and argon, respectively, and p_i and p_{Ar} are their partial pressures in the permeate. This internal-standard method allows the individual component flow rates to be determined under vacuum without interrupting the separation experiment.

The mixed-gas permeance of each component was calculated from its permeate flow rate, the effective membrane area, and the transmembrane partial-pressure difference:

$$Q_i = \frac{J_i}{A\Delta p_i}$$

where Q_i is the permeance of component *i*, J_i is the volumetric flow rate of that component through the membrane, A is the effective membrane area, and Δp_i is the difference between its partial pressures on the feed and permeate sides. The mixed-gas selectivity for a gas pair *i*/*j* was calculated as:

$$\alpha_{i/j} = \frac{Q_i}{Q_j}$$

The resulting mixed-gas permeances and selectivities were compared with the corresponding single-gas values in order to quantify the effects of competitive transport, humidification, and the presence of the other flue-gas components. The transport characteristics measured at 50 °C and feed/permeate pressures of 150/20 kPa were subsequently used as experimental input data for simulation of the membrane cascade.

For the mixed-gas permeation measurements, the analytical uncertainty of the determined component permeance did not exceed ±2.2% of the measured value. Accordingly,

propagation of the individual permeance uncertainties gives a maximum relative analytical uncertainty of approximately 3.1% for the calculated mixed-gas selectivity. Each fiber batch was characterized using 3–5 independently assembled lab-scale membrane modules, and the reported permeance and selectivity values represent the corresponding averaged values. The module-to-module deviation of the measured transport characteristics did not exceed 3.7%.

2.6. Experimental Membrane Cascade

Experimental validation of the "Continuous Membrane Column" concept was performed using a laboratory-scale membrane cascade assembled from three polysulfone hollow-fiber modules. Modules were fabricated using 63 and 32 mm polypropylene tubes and metal fitting, where the fibers were sealed with polyurea compound. The modules were interconnected according to the process configuration shown in Figure 4. The average hollow-fiber packing density in the assembled modules was approximately 45–50%.

The number of hollow fibers in each module was estimated gravimetrically. The total mass of the hollow-fiber bundle was measured, and the mass per unit length of the fiber was determined independently using representative fiber samples. The approximate number of fibers in each module, N_{fibers}, was then calculated as

$$N_{fibers} = \frac{m_{bundle}}{\lambda_{fiber} L_{fiber}}$$

where m_{bundle} is the total mass of the hollow-fiber bundle, λ_{fiber} is the experimentally determined mass per unit length of a single hollow fiber, and L_{fiber} is the fiber length used for module assembly.

The effective membrane area was calculated from the external surface area of the hollow fibers according to

$$A = N_{fibers}\, \pi\, d_o L_{active}$$

where d_o is the outer diameter of the hollow fiber and L_{active} is the effective fiber length exposed to the feed gas. The external fiber surface was used because the feed gas was supplied to the shell side of the membrane modules. The resulting effective membrane areas were 5.17 m² for M1, 0.55 m² for M2, and 0.70 m² for M3; the corresponding estimated fiber numbers and active lengths are summarized in Section 3.4.

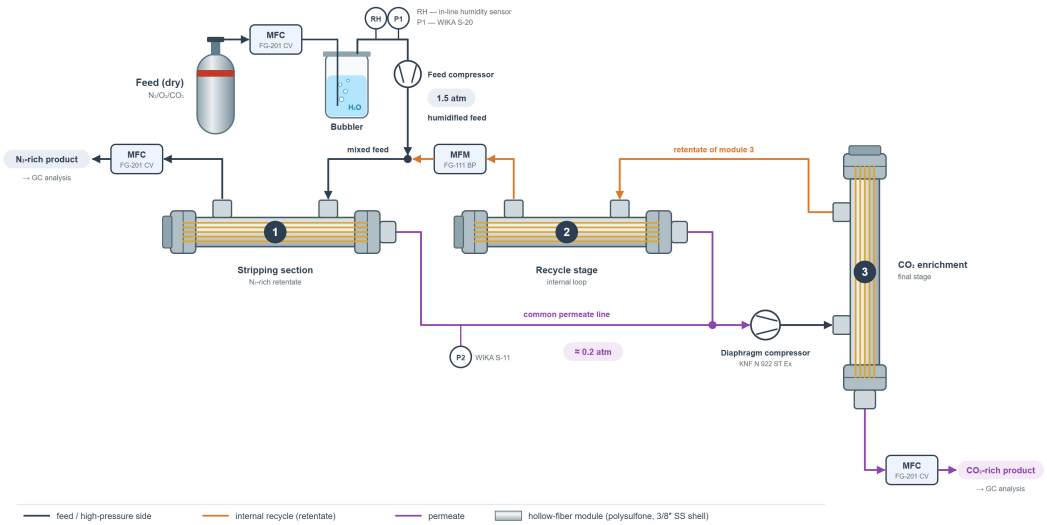


Figure 4. Principal scheme of the experimental "Continuous Membrane Column" cascade. 1–3—hollow-fiber membrane modules; MFC—mass flow controller; MFM—mass flow meter; P1, P2—pressure measurement points.

The feed mixture for the cascade experiments was prepared from a pre-mixed dry three-component gas containing N_2, O_2, and CO_2 in proportions corresponding to the dry fraction of the target flue-gas composition. The dry mixture was supplied through a mass-flow controller to a water-filled bubbler, where it was humidified to obtain the required water-vapor content. The resulting gas humidity was monitored continuously using an in-line gas humidity sensor installed downstream of the bubbler. The final wet-gas composition corresponded to $N_2/O_2/H_2O/CO_2$ = 73.0/4.4/11.0/11.6 mol.%. Before the cascade experiments, the humidification conditions and gas flow rate were adjusted until a stable water-vapor concentration was obtained. Ten replicate chromatographic determinations of the prepared feed gave H_2O concentrations of 10.94–11.07 mol.%, with a mean value of 11.0 ± 0.04 mol.%. During the experiments, feed humidity was monitored continuously using an IVTM-7 M 2-V thermohygrometer (EKSIS JSC, Moscow, Russia) with absolute accuracy ±2% RH, while periodic chromatographic measurements were used as an independent composition check.

To maintain a stable water-vapor concentration and prevent condensation within the gas-distribution system, the feed-gas cylinder, the line upstream of the bubbler, the bubbler, membrane modules, and interconnecting gas lines were maintained at 51–53 °C. The membrane modules were positioned as close to one another as practically possible and interconnected using the shortest feasible tubing lengths in order to minimize dead volume, heat losses, and condensation within the recycle and permeate lines.

The humidified feed mixture was supplied to the cascade at 1.5 atm, whereas the common permeate side of the first and second membrane modules was maintained at approximately 0.2 atm. The resulting transmembrane pressure difference provided the driving force for preferential permeation of CO_2 and H_2O through the polysulfone membranes.

The fresh feed entered the cascade at the junction between modules 1 and 2, where it was combined with the retentate stream recycled from module 2. The resulting mixed stream was introduced into module 1, which constituted the stripping section of the cascade. Preferential permeation of CO_2 through this module produced a retentate stream depleted in CO_2 and therefore enriched predominantly in nitrogen. This stream was withdrawn from the system as the N_2-rich product.

The permeate leaving module 1 was combined with the permeate generated in module 2. The combined low-pressure stream was subsequently compressed using an N 922 ST Ex diaphragm gas pump (KNF Neuberger, Germany) and supplied to module 3.

Because water vapor preferentially permeated to the low-pressure streams and became concentrated within the enrichment loop, excess moisture could condense during compression. Condensed water collected at the outlet of the N 922 ST Ex compressor was removed through an installed moisture filter before the compressed gas stream was supplied to module 3.

Module 3 served as the final CO_2-enrichment stage. Its permeate was withdrawn from the system as the CO_2-rich product stream, whereas the retentate was returned to the inlet of module 2. The retentate from module 2 was subsequently recycled to the fresh-feed mixing point upstream of module 1. Consequently, modules 2 and 3 formed an internal recirculation loop connecting the enrichment and stripping sections of the cascade. This flow arrangement reproduced the characteristic operating principle of the "Continuous Membrane Column", in which continuous internal circulation progressively enriches one stream in the preferentially permeating component while simultaneously depleting the counter-current stream.

The principal external flow rates were controlled using Bronkhorst FG-201 CV mass flow controllers (MFCs). MFCs were installed in the fresh-feed line, the N_2-rich outlet from module 1, and the CO_2-rich outlet from module 3. The internal recycle flow between the

fresh-feed mixing point and module 2 was monitored independently using a Bronkhorst FG-111 BP mass flow meter (MFM). This arrangement enabled continuous determination of the external material flows together with direct monitoring of the internal circulation rate, which is a key operating parameter of the membrane cascade.

System pressure was monitored at two characteristic locations. The pressure on the high-pressure side of the cascade was measured upstream of the membrane modules using a WIKA S-20 pressure transmitter. The reduced pressure in the common permeate line of modules 1 and 2 was monitored using a WIKA S-11 pressure transmitter.

During each experimental run, the feed composition, membrane areas, and operating pressures were kept constant, whereas the flow rates through the cascade were adjusted to investigate different operating regimes. After reaching steady state, the compositions of the two external product streams were determined. Samples of the N_2-rich retentate from module 1 and the CO_2-rich permeate from module 3 were directed to the gas chromatograph and analyzed according to the procedure described in Section 2.7. Steady-state operation was assumed after stabilization of the measured flow rates, pressures, and outlet compositions.

The experimentally measured flow rates and stream compositions were subsequently used to calculate the CO_2 concentration in the product stream, CO_2 recovery, and overall stage cut. These parameters were directly compared with the corresponding values predicted by the Aspen Plus model (Section 2.8), allowing the accuracy of the mathematical description of the "Continuous Membrane Column" cascade to be assessed under experimentally reproduced operating conditions.

The cascade experimental campaign was carried out over approximately one week using repeated daytime operating periods. During the daytime runs, steady-state separation data were collected at the selected flow conditions. At the end of each day, active gas circulation was stopped and the membrane modules and interconnecting lines were left filled with the humid model flue-gas mixture overnight; no intentional drying of the membrane modules was performed. Before measurements were resumed on the following day, the system was evacuated to an absolute pressure of approximately 0.2–0.3 bar and then refilled with fresh humid gas mixture.

2.7. Gas Chromatographic Analysis

The compositions of the membrane cascade retentate and permeate streams were determined using a two-channel gas chromatographic system equipped with thermal conductivity detectors (Figure 5). The analytical scheme was designed to provide separate quantification of CO_2 and the permanent gases, while helium was used as the carrier gas throughout the chromatographic system.

Gas samples from the membrane unit were introduced into the chromatograph through an automated valve system. One analytical channel was equipped with a HayeSep Q column, which was used to separate CO_2 from the permanent-gas fraction. The second channel included a molecular sieve 13X column for resolution of O_2 and N_2. The valve sequence was arranged so that sample injection, component separation, and back-flushing of the CO_2-containing fraction were performed automatically during each analysis cycle.

At the beginning of the chromatographic cycle, the sample filled the corresponding sampling loops. After valve switching, the gas entered the separation columns. In the first channel, the permanent-gas fraction was separated from CO_2 on HayeSep Q, after which the flow direction was reversed to remove the retained CO_2 from the column by back-flushing. In parallel, the second channel provided additional separation of CO_2 from O_2 and N_2, while the O_2/N_2 pair was subsequently resolved on the 13X molecular sieve column. Detection of the separated components was carried out using TCDs.

The concentrations of CO_2, O_2, and N_2 were calculated from the corresponding chromatographic peak areas using previously obtained calibration dependencies. For the cascade experiments, the H_2O concentration in each outlet stream was primarily determined by closure of the component balance on a wet basis, i.e., as the difference between 100 mol.% and the sum of the measured CO_2, O_2, and N_2 concentrations. The calculated water-vapor content was periodically checked using a gas-humidity analyzer. In addition, selected outlet samples were independently verified using our previously published chromatographic method, in which water vapor is quantitatively converted to acetylene on a CaC_2 precolumn and the resulting acetylene is determined chromatographically; the original H_2O content is then obtained from the reaction stoichiometry [36]. All multicomponent stream compositions reported in this work are expressed on a wet basis unless explicitly stated otherwise. The resulting component concentrations were used to determine the compositions of the retentate and permeate streams and to calculate the separation characteristics of the membrane modules and the complete cascade.

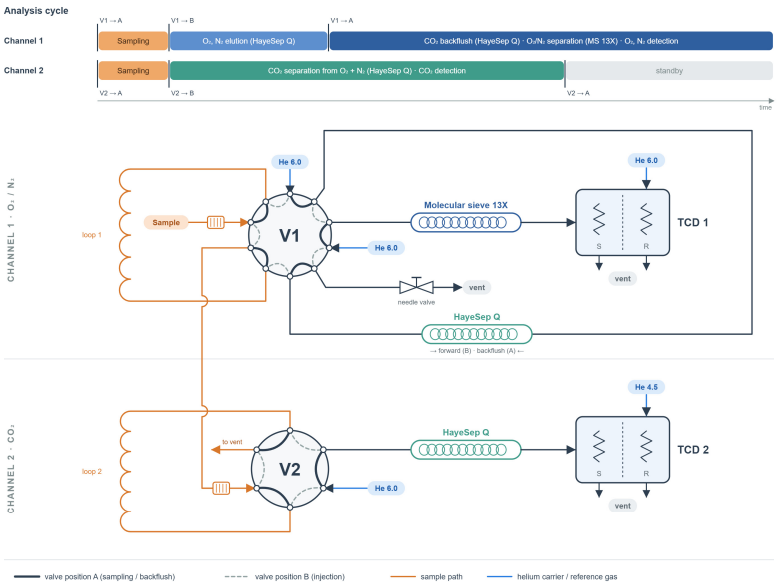


Figure 5. Schematic diagram of the two-channel gas chromatographic system used for analysis of the retentate and permeate stream compositions.

2.8. Mathematical Model and Process Simulation

The membrane-separation process was simulated in Aspen Plus using a user-defined hollow-fiber membrane block developed in Aspen Custom Modeler (ACM). The block was based on the one-dimensional steady-state Hollow Fiber Gas Permeation model developed within the U.S. Department of Energy Carbon Capture Simulation Initiative (CCSI). The original HFGP formulation is intended for multicomponent gas separation in asymmetric hollow-fiber modules and combines membrane transport equations with axial component balances and pressure-drop relationships. In the present work, the governing equations were implemented in ACM and the resulting custom membrane block was integrated into Aspen Plus, where it was connected with conventional process units and recycle streams to reproduce the investigated "Continuous Membrane Column" cascade.

The model assumes that the feed gas enters the shell side of the hollow-fiber bundle and permeates toward the fiber bores. The retentate and permeate streams are represented as counter-current one-dimensional plug flows. All fibers in a module are assumed to be identical, straight, cylindrical, and uniform in diameter. Radial concentration and velocity gradients are neglected, the gas mixture is treated as ideal, and the separation is

considered isothermal. The dense selective skin is located on the shell side, while the resistance of the porous support is neglected. The local composition at the selective-layer/porous-support boundary is therefore assumed to be equal to the bulk composition in the fiber bore. Pressure losses along both the shell and bore sides are included using Hagen-Poiseuille-type relationships for compressible gas flow.

Transport through the selective layer was described using the solution-diffusion approach. Carbon dioxide was selected as the reference component, in accordance with the original HFGP formulation. The local molar flux density of component *i* was calculated as

$$N_i = \frac{Q_{CO_2}}{\alpha_i}\left(P_{ret}Z_{ret,i} - P_{per}Z_{b,i}\right),$$

where N_i is the molar flux density of component *i*; Q_{CO_2} is the CO_2 permeance; α_i is the CO_2/i permeance selectivity; P_{ret} and P_{per} are the local pressures on the retentate and permeate sides, respectively; $Z_{ret,i}$ is the mole fraction of component *i* in the retentate; and $Z_{b,i}$ is its mole fraction at the dense-skin/porous-support boundary. Under the adopted assumptions, $Z_{b,i}$ is equal to the bulk mole fraction of component *i* in the fiber bore.

The total local molar flux density was obtained from the sum of the individual component fluxes:

$$N_t = \sum_{j=1}^{n} N_j.$$

The selectivity of the membrane relative to carbon dioxide was defined as

$$\alpha_i = \frac{Q_{CO_2}}{Q_i},$$

where Q_i is the permeance of component *i*. In the calculations, the permeance and selectivity values were specified from the experimentally determined mixed-gas transport characteristics of the produced polysulfone hollow fibers.

The spatial coordinate x was defined along the effective membrane length. The overall molar balance for the permeate flow in the fiber bore was written as

$$\frac{dF_{per}}{dx} = -J_t,$$

where F_{per} is the total molar flow rate in the permeate channel and J_t is the total molar transfer rate through the membrane per unit module length.

The pressure variation along the fiber bore was calculated from

$$P_{per}\frac{dP_{per}}{dx} = \frac{16RT\mu F_{per}}{\pi r_{FI}^4 n_F},$$

where R is the universal gas constant, T is the absolute temperature, μ is the gas viscosity, r_{FI} is the inner fiber radius, and n_F is the number of hollow fibers in the module.

For each component, the molar balance in the permeate channel was expressed as

$$\frac{dF_{c,per,i}}{dx} = -J_i,$$

where $F_{c,per,i}$ is the molar flow rate of component *i* in the permeate and J_i is the molar transfer rate of that component through the membrane per unit module length.

The corresponding overall balance on the shell side was

$$\frac{dF_{ret}}{dx} = -J_t,$$

where F_{ret} is the total molar flow rate of the retentate stream.

The shell-side pressure drop was calculated using

$$\frac{dP_{ret}}{dx} = \frac{8\mu}{r_H^2} V_{ret},$$

where r_H is the hydraulic radius of the shell-side flow channel and V_{ret} is the superficial velocity of the retentate gas.

The component balance on the shell side was written as

$$\frac{dF_{c,ret,i}}{dx} = -J_i.$$

The local component flux density was converted to the component molar transfer rate per unit module length according to

$$J_i = 2\pi r_{FO} n_F N_i,$$

where r_{FO} is the outer fiber radius. The total molar transfer rate per unit membrane length was then calculated as

$$J_t = \sum_{j=1}^{n} J_j.$$

Equations (1)–(11), together with the corresponding boundary conditions, physical-property calls, membrane dimensions, and stream specifications, form the governing equation set of the hollow-fiber membrane block. The ACM implementation uses an equation-oriented formulation, allowing both rating and design calculations depending on which model variables are fixed to close the degrees of freedom.

The axial domain was solved by the method of lines. Following the HFGP model structure, the membrane length was discretized using a second-order centered finite-difference approximation with 20 axial elements. The resulting nonlinear steady-state equation system was solved by ACM. The completed user block was subsequently exported to Aspen Plus and employed as the membrane module in the process flowsheet.

The process calculations were performed for the wet model flue gas used in the experimental study, containing 73.0 mol.% N_2, 4.4 mol.% O_2, 11.0 mol.% H_2O, and 11.6 mol.% CO_2. The temperature was fixed at 50 °C. The shell-side feed pressure and bore-side permeate pressure were set to 150 and 20 kPa, respectively. The experimentally obtained mixed-gas permeances of CO_2, N_2, O_2, and H_2O were used as membrane input parameters. In the base-case simulations, the experimentally determined mixed-gas transport parameters were treated as composition-independent constants. To evaluate the sensitivity of the predicted process performance to this assumption, additional lab-scale calculations were performed with membrane permeance and selectivity varied independently by ±10% and ±20% relative to the base case. For the permeance sensitivity analysis, the component permeances were varied proportionally while preserving the baseline selectivity ratios. For the selectivity sensitivity analysis, the CO_2 permeance was maintained at its baseline value, while the permeances of the less selectively permeating components were adjusted to obtain the prescribed ±10% and ±20% changes in CO_2 selectivity. All other process parameters, including membrane areas, feed composition, pressure conditions, feed-flow range, and cascade topology, were kept unchanged.

For analysis of individual membrane stages, the stage cut was defined as

$$\theta = \frac{F_p}{F_f},$$

where F_p and F_f are the total permeate and feed molar flow rates, respectively.

Carbon-dioxide recovery in the product stream was calculated as

$$R_{CO_2} = \frac{F_p y_{CO_2,p}}{F_f x_{CO_2,f}} \times 100\%,$$

where $x_{CO_2,f}$ and $y_{CO_2,p}$ are the CO_2 mole fractions in the feed and product streams, respectively.

The CO_2 purity of the product stream was expressed as

$$C_{CO_2} = y_{CO_2,p} \times 100\%.$$

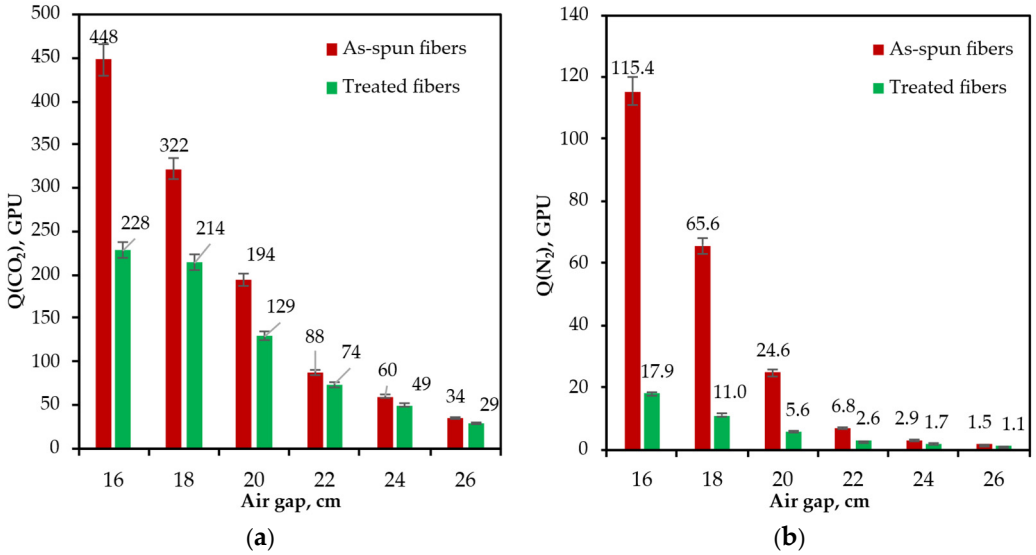
For the complete "Continuous Membrane Column" flowsheet, the same material-transfer model was used for each membrane section, while the membrane areas of the stripping and enrichment sections were varied parametrically. Aspen Plus simultaneously solved the material balances of the interconnected membrane modules and recycle streams. For each combination of membrane areas, the product CO_2 concentration, CO_2 recovery, residual CO_2 concentration in the vent stream, and internal recycle flow rates were calculated. The resulting dependencies were used to identify the membrane-area combinations suitable for subsequent experimental validation of the cascade.

3. Results and Discussion

3.1. Single-Gas Permeation and Fiber Post-Treatment

The single-gas permeation results revealed a pronounced dependence of the transport characteristics of the asymmetric PSF hollow fibers on the air-gap distance used during spinning (Figure 6). Measurements were performed for CO_2, O_2, and N_2 according to the procedure described in Section 2.4, while the same membrane batches were characterized both in the as-spun state and after defect healing with Sylgard™ 184.

For the untreated fibers, increasing the air gap from 16 to 26 cm resulted in a continuous and substantial decrease in gas permeance. The CO_2 permeance decreased from approximately 448 GPU at an air gap of 16 cm to 322, 194, 88, 60, and 34 GPU at 18, 20, 22, 24, and 26 cm, respectively. A similar trend was observed for the less permeable gases. The N_2 permeance decreased from 115.4 to 1.5 GPU over the same range, while the O_2 permeance decreased from approximately 134 to 7 GPU. Thus, increasing the residence time of the nascent fiber in the air gap progressively increased the resistance of the outer selective layer.



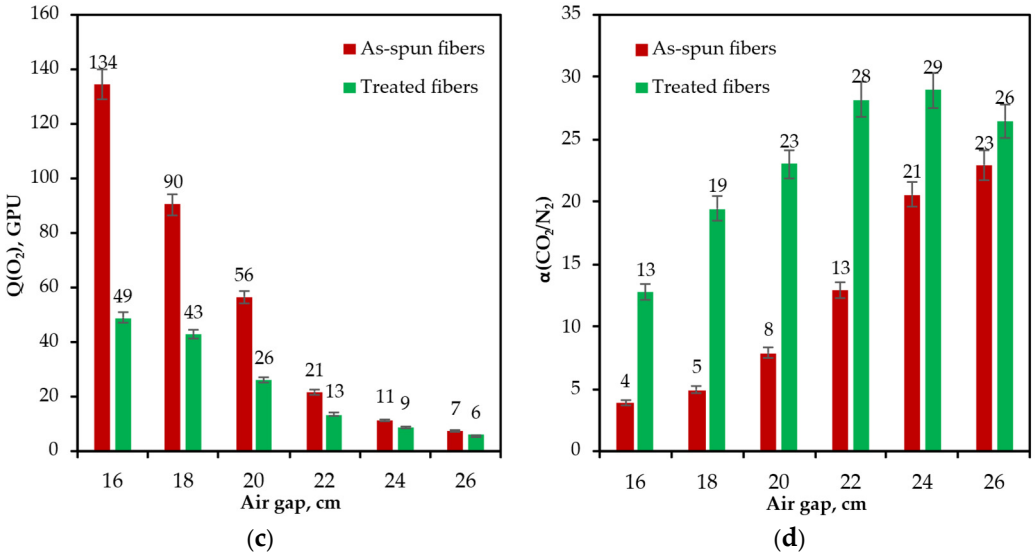


Figure 6. Gas transport characteristics of spun PSF hollow fibers: as-spun and silicone treated samples. (**a**–**c**) hollow fiber permeance with regard to CO_2, N_2 and O_2; (**d**) hollow fibers selectivity to CO_2/N_2 pair.

The replicate CO_2 permeance measurements yielded standard deviations of 13.4, 6.8, 4.4, 3.4, 2.1, and 1.3 GPU for air gaps of 16, 18, 20, 22, 24, and 26 cm, respectively, corresponding to relative standard deviations of approximately 2.1–3.9%. Thus, the overall decrease from 447.6 ± 13.4 GPU at 16 cm to 34.4 ± 1.3 GPU at 26 cm (approximately 92%) was far greater than both the experimental dispersion and the estimated instrumental uncertainty. The monotonic dependence of CO_2 permeance on air-gap distance was statistically significant (Spearman rank correlation $\varrho = -1.00$, two-sided $p = 0.0028$).

The simultaneous evolution of permeance and selectivity indicates that the effect of the air gap cannot be described solely as an increase in selective-layer thickness. At short air-gap distances, the outer skin remained highly permeable but contained a significant population of non-selective defects. This is particularly evident from the O_2/N_2 permeance ratio. For the fibers spun with air gaps of 16 and 18 cm, $\alpha(O_2/N_2)$ was only approximately 1.2 and 1.4, respectively. These values are close to non-selective transport and are far below the intrinsic O_2/N_2 selectivity of dense polysulfone. Consequently, the exceptionally high permeances of these batches cannot be attributed exclusively to an ultrathin but continuous PSF selective layer; a considerable fraction of the total gas flow must instead pass through pinholes or other highly permeable defects.

This interpretation is consistent with the classical observations of Pinnau and Koros for integrally skinned asymmetric polysulfone membranes. They showed that wet-phase-inverted PSF membranes containing skin defects can exhibit O_2/N_2 selectivities below unity or close to unity, whereas dry/wet phase inversion under conditions promoting formation of a continuous skin produced membranes with selectivities approaching those of dense polysulfone films [37]. In their work, an asymmetric membrane was considered essentially defect-free when its O_2/N_2 selectivity reached approximately 85% or more of that measured for the corresponding dense polymer.

A distinct transition toward solution–diffusion-controlled transport was observed beginning at an air gap of approximately 20 cm. For this batch, the untreated fiber retained a relatively high CO_2 permeance of approximately 194 GPU, while $\alpha(O_2/N_2)$ increased to approximately 2.3. Further extension of the air gap to 22, 24, and 26 cm progressively increased $\alpha(O_2/N_2)$ to approximately 3.1, 3.8, and 4.7, respectively. The corresponding CO_2/N_2 selectivity increased even more markedly, from approximately 7.9 at 20 cm to 12.9, 20.6, and 22.9 at 22, 24, and 26 cm. These results indicate a progressive transition from

defect-dominated permeation toward transport increasingly governed by the intrinsic sorption–diffusion properties of the PSF matrix.

The observed behavior is physically consistent with the dry–wet spinning mechanism. Increasing the air gap prolongs the period between extrusion and immersion of the nascent fiber into the coagulation bath. During this interval, preferential evaporation of the volatile THF component and redistribution of solvent and non-solvent near the external surface promote polymer enrichment and consolidation of the outer skin. Consequently, longer air gaps favor formation of a more continuous and less defective selective layer, but simultaneously increase its resistance to gas transport. This interpretation is particularly relevant to the PSF/DMF/THF/IPA system employed here, in which THF was intentionally introduced as a volatile co-solvent affecting skin formation.

The gas-transport behavior of the more selective fibers can be compared with published data for the same commercial polysulfone grade. Kluge et al. investigated P-3500 LCD MB7 supplied by Solvay. For a dense reference membrane, they reported permeabilities of 6.18 Barrer for CO_2, 1.05 Barrer for O_2, and 0.20 Barrer for N_2, corresponding to $\alpha(CO_2/N_2) = 30.9$ and $\alpha(O_2/N_2) = 5.4$. Depending on membrane preparation conditions, PSF membranes in the same study exhibited CO_2/N_2 selectivities of approximately 30.9–37.5 and O_2/N_2 selectivities of 5.4–7.1 [38]. These literature data provide a useful intrinsic-performance benchmark but should not be regarded as a strict universal value, because membrane morphology and formation history can substantially affect the transport properties of thin PSF selective layers.

A similar conclusion was reached in the fundamental studies of Koros and co-workers. Pesek and Koros obtained aqueous-quenched asymmetric PSF membranes with ultrathin, essentially defect-free selective layers of approximately 200–800 Å that retained intrinsic polymer permselectivity without requiring a silicone coating [39]. In a subsequent study specifically devoted to asymmetric PSF hollow fibers, Pesek and Koros reported fibers with an approximately 120 nm selective skin, an O_2 permeance of 8.8 GPU, and $\alpha(O_2/N_2) = 5.8$, demonstrating that intrinsic-like selectivity can also be achieved in hollow-fiber geometry when the selective surface is essentially defect-free [40].

Silicone post-treatment caused a fundamentally different change in transport characteristics than increasing the air gap. After Sylgard™ 184 treatment, the permeance of all gases decreased, but the decrease was strongly gas-dependent and was most pronounced for N_2. For the 16 cm batch, for example, CO_2 permeance decreased from approximately 448 to 228 GPU, whereas N_2 permeance decreased much more strongly, from 115.4 to 17.9 GPU. Consequently, $\alpha(CO_2/N_2)$ increased from approximately 3.9 to 12.7. At an air gap of 18 cm, CO_2 permeance decreased from approximately 322 to 214 GPU, while N_2 permeance fell from 65.6 to 11.0 GPU, increasing $\alpha(CO_2/N_2)$ from approximately 4.9 to 19.5.

Such disproportionate suppression of the N_2 flux provides strong evidence that the silicone treatment primarily sealed non-selective transport pathways rather than simply adding a uniform additional resistance to the entire membrane surface. If a thick PDMS layer had become the principal separation medium, the measured selectivities would tend toward those characteristics of PDMS. Kluge et al., for example, reported $\alpha(CO_2/N_2) \approx 10.3$ and $\alpha(O_2/N_2) \approx 2.1$ for the PDMS coating material itself [38]. The substantially higher selectivities obtained here for the treated fibers with air gaps ≥ 20 cm therefore indicate that separation remained governed predominantly by the underlying PSF skin, whereas the silicone layer acted mainly as a defect-healing phase.

The most favorable balance between productivity and separation efficiency was obtained for the fibers spun at an air gap of 20 cm. Silicone treatment reduced the CO_2 permeance from approximately 194 to 129 GPU, while N_2 permeance decreased from 24.6 to 5.6 GPU and O_2 permeance from approximately 56 to 26 GPU. As a result, $\alpha(CO_2/N_2)$ increased from approximately 7.9 to 23, whereas $\alpha(O_2/N_2)$ increased from approximately 2.3

to 4.6. The latter corresponds to approximately 85–86% of the O_2/N_2 selectivity of 5.4 reported for dense P-3500 LCD MB7 polysulfone by Kluge et al. [38], satisfying the criterion proposed by Pinnau and Koros for an essentially defect-free asymmetric selective skin.

Further increase in the air gap produced higher selectivities but at the expense of a pronounced decrease in membrane productivity. After silicone treatment, $\alpha(CO_2/N_2)$ increased to approximately 28 and 29 for the 22 and 24 cm batches, respectively, while their CO_2 permeances decreased to only approximately 74 and 49 GPU. For the 26 cm batch, the CO_2 permeance decreased further to approximately 29 GPU, whereas $\alpha(CO_2/N_2)$ remained around 26. Thus, beyond an air gap of approximately 20–22 cm, further improvement in skin integrity provided progressively smaller benefits in selectivity relative to the loss in permeance. The slight decrease in CO_2/N_2 selectivity observed at 26 cm also suggests that once the contribution of macroscopic defects becomes small, additional increases in skin thickness or changes in the morphology of the near-surface polymer no longer necessarily improve the intrinsic discrimination between CO_2 and N_2.

The same conclusion is supported by the O_2/N_2 results. After silicone treatment, $\alpha(O_2/N_2)$ increased from approximately 2.7 and 3.9 for the 16 and 18 cm fibers to approximately 4.6, 5.0, 5.3, and 5.5 for the 20–26 cm batches. The latter values approach the range reported for dense and essentially defect-free polysulfone membranes. Pinnau and Koros reported that properly formed dry/wet asymmetric PSF membranes retained at least approximately 85% of dense-film O_2/N_2 selectivity [37], while Pesek and Koros obtained $\alpha(O_2/N_2) = 5.8$ for defect-free aqueous-quenched PSF hollow fibers [40].

A quantitative comparison of Figure 6 data further illustrates this trade-off. For the untreated fibers, increasing the air gap from 16 to 26 cm decreased the CO_2 permeance from 448 to 34 GPU (approximately 92%), the N_2 permeance from 115.4 to 1.5 GPU (approximately 99%), and the O_2 permeance from approximately 134 to 7 GPU (approximately 95%). For the 20 cm fiber, Sylgard treatment decreased CO_2 permeance from 194 to 129 GPU (approximately 34%), whereas N_2 permeance decreased much more strongly, from 24.6 to 5.6 GPU (approximately 77%); consequently, $\alpha(CO_2/N_2)$ increased from 7.9 to approximately 23, i.e., by about 2.9-fold (approximately 191%). Further increasing the air gap from 20 to 24 cm raised $\alpha(CO_2/N_2)$ only from approximately 23 to 29 (about 26%), while CO_2 permeance fell from 129 to 49 GPU (approximately 62%). At 26 cm, CO_2 permeance decreased to approximately 29 GPU (approximately 78% below the 20 cm value), without any further gain in CO_2/N_2 selectivity. Thus, the 20 cm condition was selected because it preserved substantially higher productivity while already providing a largely defect-healed selective skin and near-intrinsic O_2/N_2 discrimination.

Overall, the results demonstrate that the air-gap distance controls a clear permeance–selectivity transition in the as-spun fibers, whereas silicone treatment provides an additional means of selectively suppressing defect-mediated transport. Short air gaps of 16–18 cm yield highly productive but strongly defective fibers; long air gaps of 22–26 cm produce substantially more selective skins but at the cost of increasingly low permeance. The 20 cm air gap therefore represents the most attractive compromise for further process development: after defect healing, the fibers retained a CO_2 permeance of approximately 129 GPU, while achieving $\alpha(CO_2/N_2) \approx 23$ and $\alpha(O_2/N_2) \approx 4.6$. This batch and 22, 24 air gap batches were consequently selected for subsequent mixed-gas characterization and experimental evaluation of the membrane cascade.

The SEM micrographs (Figure 7) confirm the structural evolution of the hollow-fiber wall with increasing air-gap distance. Fibers prepared at 16 cm exhibit pronounced finger-like macrovoids extending close to the external surface and a relatively open near-wall region, which is consistent with their very high permeance and low O_2/N_2 and CO_2/N_2 selectivities. At 18 cm, the near-surface structure becomes somewhat denser, although large macrovoids remain clearly visible. A more substantial morphological change is

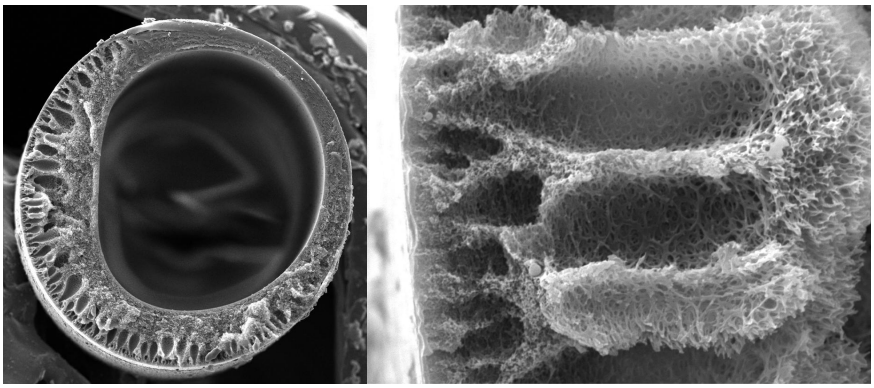
observed at 20 cm, where the wall contains a larger fraction of sponge-like structure and the outer region appears more consolidated.

Quantitative analysis of the SEM cross-sections provides additional support for this interpretation. The lumen diameter remained nearly constant at approximately 320–330 μm over the investigated range, whereas the outer fiber diameter and wall thickness decreased with increasing air-gap distance, indicating progressive elongational drawing of the nascent fiber before coagulation. The 18 cm air gap fiber also exhibited pronounced eccentricity of the lumen: the wall thickness was approximately 25–30 μm on the thinner side and approximately 80 μm on the opposite side. This asymmetry is consistent with a slight spinneret misalignment and/or non-uniform dope flow during spinning. For the 20 cm air-gap fibers selected for the cascade experiments, the outer diameter was approximately 430–450 μm, while the lumen diameter remained approximately 320–330 μm.

The internal morphology changed quantitatively from a macrovoid-rich to a predominantly sponge-like structure. At an air gap of 16 cm, finger- and teardrop-shaped macrovoids were typically approximately 8–15 μm wide and extended for more than 30 μm in the radial direction; the macrovoid-rich zone reached approximately 40–60 μm into the wall. At 18 cm, the macrovoids became less abundant and shorter, with typical dimensions of approximately 5–15 μm and occasional larger cavities of approximately 30–40 μm. In contrast, the 20 cm fiber exhibited an almost entirely sponge-like wall with characteristic pores of approximately 0.2–1 μm and only isolated cavities not exceeding approximately 5 μm. A compact region of about 1 μm is visible at the external surface; however, this apparent layer should not be interpreted as the true selective-skin thickness, because the SEM magnification used here is insufficient to resolve the ultrathin gas-selective layer reliably. The progressive suppression of macrovoids is consistent with increasing polymer enrichment and delayed phase separation during the longer residence time in the air gap, and it agrees with the simultaneous decrease in permeance and increase in selectivity observed in Figure 6.

This trend agrees with the gas-transport data: increasing the air gap reduces permeance while increasing selectivity, indicating a transition from defect-dominated transport toward transport increasingly governed by the solution–diffusion mechanism. Similar effects of the dry-step duration on the formation and integrity of the selective skin in asymmetric polysulfone membranes were reported by Pinnau and Koros [37,41].

The 20 cm fiber provides the most favorable balance between morphology and transport performance. After Sylgard treatment, its CO_2 permeance remained relatively high at about 129 GPU, while $\alpha(CO_2/N_2)$ increased to approximately 23 and $\alpha(O_2/N_2)$ to about 4.6. These results indicate that the silicone layer mainly sealed residual surface defects rather than acting as an independent selective layer.



(**a**) (**b**)

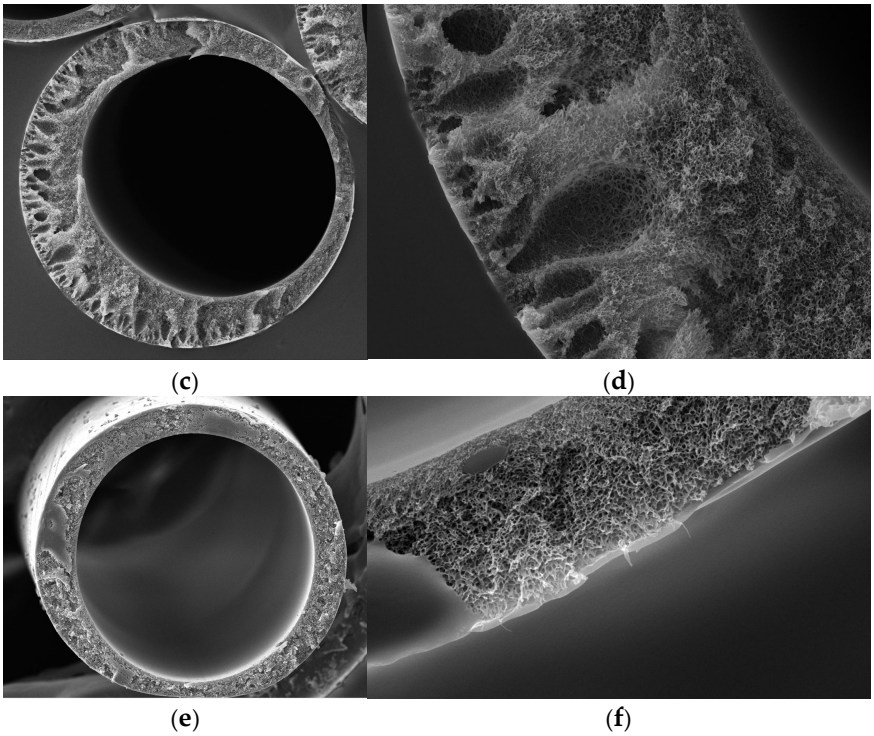
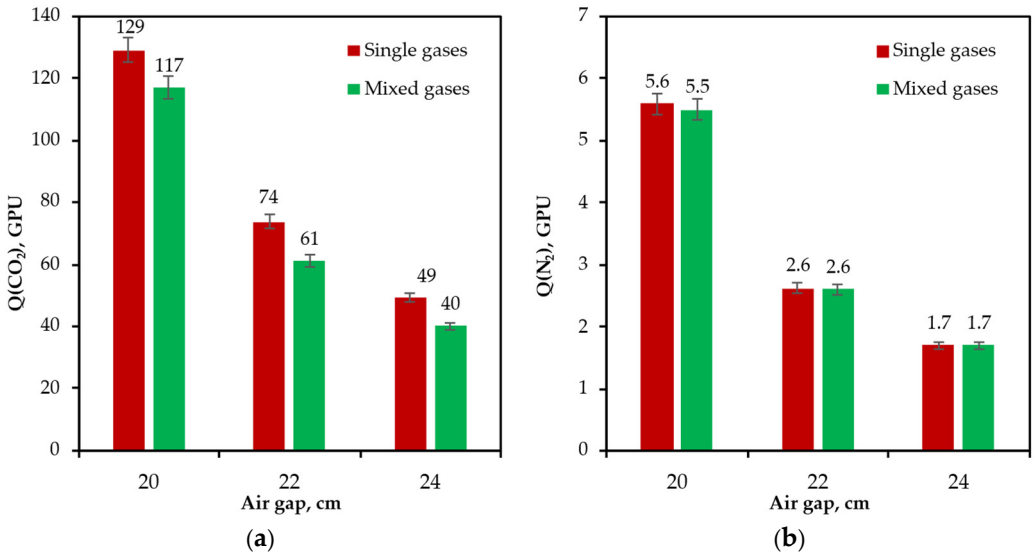


Figure 7. SEM micrographs of asymmetric PSF hollow fibers prepared at air-gap distances of (**a**,**b**) 16 cm, (**c**,**d**) 18 cm, and (**e**,**f**) 20 cm. Images (**a**,**c**,**e**) show the complete fiber cross-sections, whereas (**b**,**d**,**f**) show enlarged views of the external near-wall region.

3.2. Mixed-Gas Permeation

The mixed-gas permeation behavior of the selected Sylgard-treated PSF hollow fibers was evaluated using the humid model flue gas containing $N_2/O_2/H_2O/CO_2$ = 73.0/4.4/11.0/11.6 mol.% at 50 °C and a feed-to-permeate pressure gradient of 130 kPa, respectively (Figure 8). The results show that exposure to the multicomponent mixture caused a moderate but systematic decrease in the permeance of CO_2 and O_2, whereas N_2 permeance remained essentially unchanged.



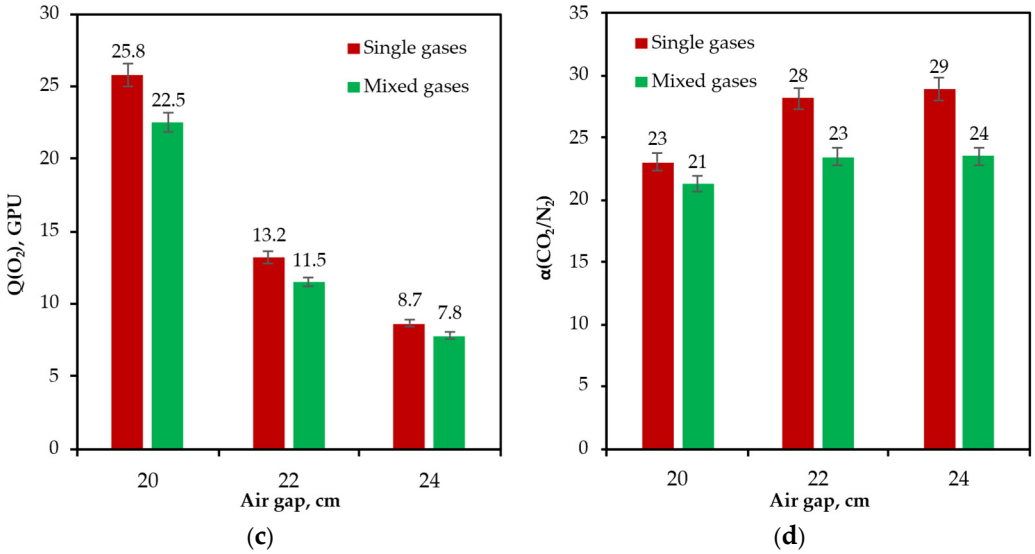


Figure 8. Gas transport characteristics of spun PSF hollow fibers: single gas and mixed gases. (**a–c**) hollow fiber permeance with regard to CO_2, N_2 and O_2; (**d**) hollow fibers selectivity to CO_2/N_2 pair.

For the fiber prepared at an air gap of 20 cm, the CO_2 permeance decreased from 129 GPU for the pure gas to 117 GPU in the mixed-gas experiment, corresponding to a reduction of approximately 9%. The decrease became more pronounced for the denser fibers: from 74 to 61 GPU for the 22 cm batch and from 49 to 40 GPU for the 24 cm batch, i.e., reductions of approximately 18% in both cases. Oxygen showed a similar trend, with permeance decreasing from 25.8 to 22.5 GPU, from 13.2 to 11.5 GPU, and from 8.7 to 7.8 GPU for the 20, 22, and 24 cm fibers, respectively. In contrast, N_2 permeance changed only marginally, from 5.6 to 5.5 GPU for the 20 cm sample and remaining essentially constant at 2.6 and 1.7 GPU for the 22 and 24 cm samples.

The reduction in CO_2 permeance caused a corresponding decrease in effective CO_2/N_2 selectivity. For the 20 cm fiber, $\alpha(CO_2/N_2)$ decreased from approximately 23 under pure-gas conditions to 21.3 in the wet mixture. For the 22 and 24 cm samples, the selectivity decreased from approximately 28–29 to 23.5. Despite this reduction, all three membranes retained substantial preferential transport of CO_2 over N_2, indicating that the defect-healed selective layer remained effective under humid multicomponent conditions. The moderate loss in selectivity also illustrates why process simulations based only on pure-gas permeances can overestimate actual membrane performance under flue-gas conditions.

A particularly important feature of the mixed-gas experiments was the very high permeance of water vapor. Although H_2O is not included in Figure 8 because its permeance was substantially higher than that of the permanent gases, the measured values were 525 ± 30, 390 ± 25, and 310 ± 20 GPU for the fibers spun at 20, 22, and 24 cm, respectively. These values correspond to H_2O/CO_2 permeance ratios of approximately 4.5, 6.4, and 7.8. High water-vapor transport through PSF has been reported previously and reflects the strong condensability and sorption affinity of water compared with N_2 and O_2. Measurements of water-vapor/inert-gas mixtures through polysulfone films have likewise shown that water transport can greatly exceed that of permanent gases [42].

Possible capillary condensation of water within the porous hollow-fiber substructure and water-induced plasticization of the PSF selective region were not quantified independently in the present study. Local condensation within the sponge-like porous support cannot therefore be completely excluded. Nevertheless, the experimentally observed transport response does not indicate a strongly pronounced effect of either liquid-water pore filling or plasticization under the investigated conditions. In the humid mixed gas,

CO_2 permeance decreased by only approximately 9% for the 20 cm fiber and by about 18% for the 22 and 24 cm fibers, whereas N_2 permeance remained essentially unchanged and CO_2/N_2 selectivity decreased only moderately. Thus, even if capillary condensation or water-induced changes in the polymer structure were present locally, their overall influence on the measured membrane transport characteristics appears limited within the investigated operating range. Dedicated experiments with systematically varied water activity would be required to quantify these effects separately.

The decrease in H_2O permeance with increasing air gap follows the same general trend observed for CO_2 and O_2 and is consistent with the progressive densification of the selective region discussed in Section 3.1. Similar behavior was observed for dry–wet-spun PSF hollow fibers tested with the same humid flue-gas composition, where water-vapor permeance remained the highest among all components and varied strongly with membrane morphology [43]. Thus, increasing the air gap reduces the overall transport rate of all condensable species, but the relative preference for H_2O becomes stronger as the membrane becomes denser.

From a process perspective, the high H_2O permeance has two consequences. First, water vapor will preferentially follow CO_2 to the permeate side of the cascade and therefore must be explicitly included in the membrane model rather than treated as an inert feed component. Second, the high H_2O/CO_2 permeance ratio means that the CO_2-rich permeate can also become strongly enriched in water, which may affect downstream compression and condensation. For this reason, the experimentally determined mixed-gas permeances, rather than the corresponding pure-gas values, were used as input parameters for the process simulation.

A strictly like-for-like comparison with literature data is difficult because only a limited number of studies report hollow-fiber or thin-film composite membrane performance using humid mixed gases at post-combustion-relevant CO_2 concentrations. The closest PSF hollow-fiber benchmark is our previous study [43], in which the same wet $N_2/O_2/H_2O/CO_2$ = 73.0/4.4/11.0/11.6 mol.% mixture was used, although at 25 °C rather than 50 °C. Table 2 therefore compares the present membrane with this closest PSF dataset and with representative thin-film composite membranes tested under humid mixed-gas or real wet-flue-gas conditions.

Table 2. Comparison of CO_2/N_2 transport performance for the present PSF hollow fiber and selected membranes evaluated under humid or wet mixed-gas conditions.

Membrane	Wet Mixed-Gas Conditions	T/P	Q(CO_2), GPU	$\alpha(CO_2/N_2)$
PSF Present study	$N_2/O_2/H_2O/CO_2$ 73.0/4.4/11.0/11.6 mol.%	50 °C; feed pressure 150 kPa	117	21.3
PSF Țiuleanu et al. [43]	$N_2/O_2/H_2O/CO_2$ 73.0/4.4/11.0/11.6 mol.%	25 °C; feed pressure 150 kPa	70.1–1047	3.3–18.8
PolyActive/PDMS/PES Chou et al. [44]	CO_2/N_2 15/85 at 50% RH	25 °C; feed pressure 200 kPa	413	20.24
GO-reinforced PAM/PVA/PSf Chen et al. [45]	Humidified CO_2/N_2 10/90	30 °C; feed pressure 200 kPa	55	65
Pohlmann et al. [26] PolyActive pilot module	Real wet coal-fired power-plant flue gas	20 °C; feed pressure 110 kPa	≈1062	≈43

The closest PSF comparison [43] shows that the present defect-healed fiber occupies the high-selectivity end of the PSF hollow-fiber performance range under the same wet feed composition. Relative to the most selective PSF sample reported in that study (Q(CO_2)

= 70.1 GPU, $\alpha(CO_2/N_2)$ = 18.8), the present membrane provides approximately 67% higher CO_2 permeance and approximately 13% higher CO_2/N_2 selectivity, although the different test temperatures (50 versus 25 °C) preclude a strict one-to-one comparison. The recent humid PolyActive/PDMS/PES TFC hollow fiber reported by Chou et al. shows a similar CO_2/N_2 selectivity (20.24 versus 21.3) but a substantially higher CO_2 permeance (413 versus 117 GPU). In contrast, the GO-reinforced PAM/PVA/PSf thin-film composite membrane reported by Chen et al. under humidified 10/90 CO_2/N_2 conditions exhibited a lower CO_2 permeance of 55 GPU but a substantially higher CO_2/N_2 selectivity of 65, illustrating the usual permeance–selectivity trade-off. Established PolyActive pilot-scale TFC membranes provide still higher transport performance, with representative values around 1062 GPU and $\alpha(CO_2/N_2) \approx 43$ under wet flue-gas operation [26]. Accordingly, the present PSF hollow fiber should not be regarded as a record-performance membrane; its relevance lies in combining moderate but reproducible wet mixed-gas selectivity with a simple, scalable integrally skinned hollow-fiber architecture that can be directly incorporated into the experimentally validated cascade.

Overall, the mixed-gas results confirm that the 20 cm fiber remains the most favorable compromise between productivity and selectivity. It retains a comparatively high CO_2 permeance of 117 GPU together with $\alpha(CO_2/N_2)$ = 21.3 and $\alpha(O_2/N_2)$ = 4.1, whereas the 22 and 24 cm fibers provide only a modest gain in mixed-gas selectivity at the expense of substantially lower CO_2 permeance. Consequently, the 20 cm membrane was selected for subsequent process calculations and experimental validation of the membrane cascade.

3.3. Process Simulation

The experimentally determined mixed-gas permeances of the PSF hollow-fiber membrane were introduced into the Aspen Plus model to evaluate the performance of the "Continuous Membrane Column" cascade under conditions corresponding to the subsequent laboratory experiments in terms of pressure and temperature. A scaled-down representative flue-gas flow rate of 100 L(N) min^{-1} was used as the overall feed flow in the process simulation. Other details of process simulation conditions are given in Table 3. Three process criteria were considered: a CO_2 recovery above 80%, a CO_2 concentration in the residual stream below 2 mol.%, and a CO_2 concentration in the product stream above 70 mol.%. These requirements are intentionally less stringent than the targets commonly adopted for post-combustion carbon capture, where CO_2 recovery of at least 90%, product purity above 95 mol.%, and residual CO_2 below 2 mol.% are typically considered. In our previous studies [34,35], however, it was demonstrated that achievement of these more demanding targets is strongly limited by membrane selectivity. For a binary CO_2/N_2 mixture, a CO_2/N_2 selectivity of at least approximately 32 was required to obtain a product purity above 95 mol.%, whereas for the realistic four-component wet flue gas the required selectivity increased to approximately 48.

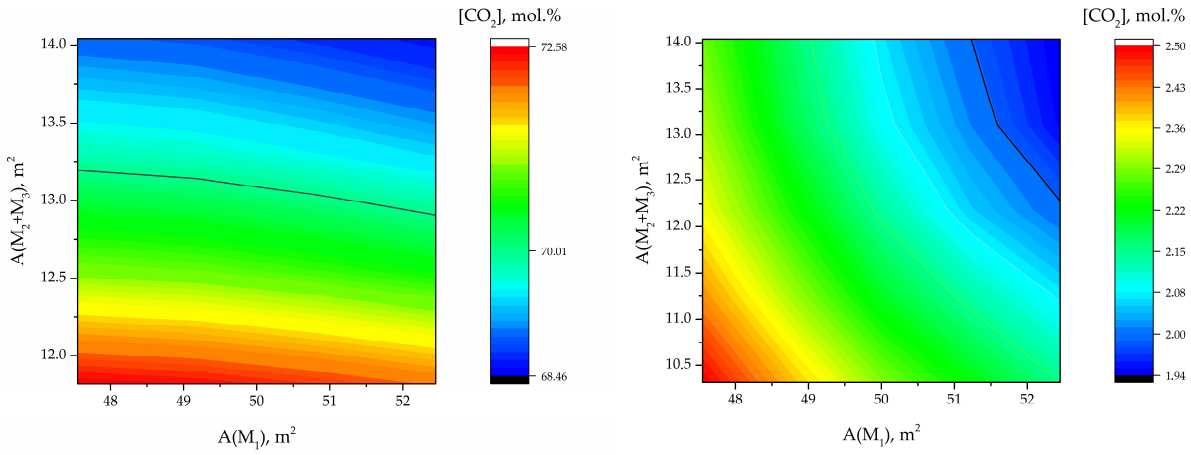
Two complementary simulation cases were considered in the present work. The first, hereafter referred to as the process-scale simulation, was used for process analysis and membrane-area sensitivity calculations and employed a representative feed flow of 100 L(N) min^{-1}. The second, hereafter referred to as the lab-scale simulation, was introduced specifically for direct verification against the experimental cascade. In this case, the model used the actual membrane areas of the laboratory modules (5.17 m^2 for M1, 0.55 m^2 for M2, and 0.70 m^2 for M3) together with the experimentally investigated feed-flow range of 5.7–10 L(N) min^{-1}. Feed composition, temperature, pressure conditions, membrane transport parameters, and cascade topology were kept identical in the two calculations. This additional lab-scale calculation therefore allowed the influence of absolute process scale and module geometry to be separated from deviations associated with the idealized description of the real experimental system.

Table 3. Process simulation parameters.

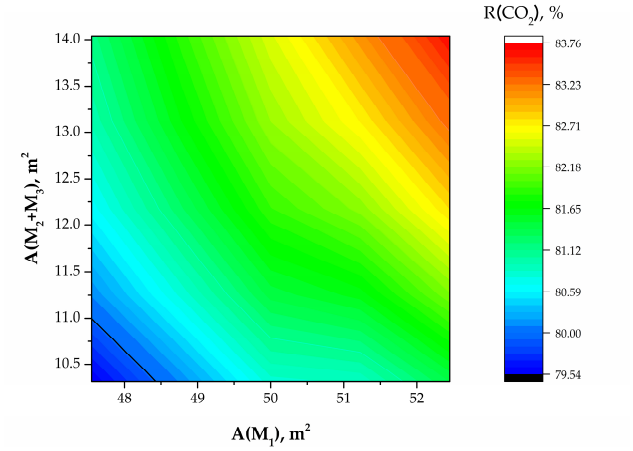
Parameter	Value
Feed flow, L(N) min^{-1}	100
Pressure, MPa	0.15
Temperature, °C	50
Flue gas composition, mol.%	
N_2	73
CO_2	11.6
H_2O	11
O_2	4.4

The present PSF membrane exhibits substantially lower mixed-gas selectivity and therefore cannot be expected to reproduce the separation performance predicted previously for high-performance CO_2-selective membranes merely by increasing membrane area. This point is important because the membrane area primarily controls the stage cut and the amount of gas transferred between the retentate and permeate streams, whereas insufficient intrinsic selectivity leads to simultaneous permeation of N_2 and O_2 together with CO_2. In the previous four-component simulation, it was shown that membranes with CO_2/N_2 selectivity of approximately 20–21 were unable to meet the stringent residual-CO_2 specification while maintaining high product purity, and a selectivity close to 48 was required to reach 95 mol.% CO_2 in the product stream.

The effect of the membrane areas in the stripping and enrichment sections is illustrated in Figure 9 by two-dimensional response maps. Increasing the membrane area in module M1 produces the most direct effect on CO_2 removal from the feed stream. A larger membrane area of first module increases the stage cut in the stripping section and, consequently, increases the amount of CO_2 transferred to the permeate side. As a result, CO_2 recovery increases and the CO_2 concentration in the residual stream decreases. This behavior is consistent with the mechanism previously established for the "Continuous Membrane Column": M1 determines the extent of CO_2 removal from the original flue-gas stream and simultaneously controls the composition and flow rate entering the enrichment part of the cascade.



(**a**) (**b**)



(**c**)

Figure 9. Two-dimensional response maps showing the simultaneous effect of the stripping-section membrane area, A(M_1), and the total enrichment-section membrane area, A(M_2+M_3), on (**a**) CO_2 concentration in the product stream, (**b**) CO_2 concentration in the residual stream, and (**c**) CO_2 recovery. The highlighted contour lines indicate the corresponding process-performance limits.

The recovery map shows that the recovery criterion is the least restrictive of the three considered requirements. CO_2 recovery increases from approximately 79.5% at the lowest membrane areas to almost 84% at the upper end of the investigated range. The recovery rate of 80% boundary is reached already at relatively small membrane areas, after which further increases in either in membrane area of both sections provide only a gradual increase in recovery. Thus, for the investigated PSF membrane, the 80% recovery target can be achieved over most of the considered membrane-area range.

For quantitative reference, the response maps in Figure 9 cover a stripping-section membrane area A(M1) of approximately 47.5–52.5 m^2 and a total enrichment-section area A(M2+M3) of approximately 10.5–14.0 m^2. At the lower-area corner of this domain, the model gives a CO_2 recovery of about 79.5%, a product CO_2 concentration of approximately 72.1 mol.%, and a residual CO_2 concentration of about 2.4 mol.%. At the upper-area corner, the corresponding values are approximately 83.8%, 68.9 mol.%, and 1.94 mol.%, respectively. The low- and high-utilization process-scale cases that bracket this range correspond to overall stage cuts of approximately 0.11 and 0.19, respectively. These numerical values make explicit the recovery–purity trade-off represented by the response surfaces.

An increase in the membrane area of the enrichment section also increases CO_2 recovery, but through a different mechanism. Larger membrane areas in M2 and M3 allow a greater fraction of the CO_2 transferred from the stripping section to be retained on the product side of the cascade rather than returned through the internal recycle. Accordingly, increasing membrane area of the M2 and M3 reduces CO_2 circulation back toward M1 and lowers CO_2 losses in the residual stream. Similar coupling between the stripping and enrichment sections was observed in the previous simulations: insufficient membrane area in the enrichment section increased the CO_2 recycle load and consequently required a larger stripping-section area to obtain the same overall separation performance.

The residual-stream composition is therefore governed by the simultaneous action of both membrane sections. Increasing module 1 membrane area directly removes a larger fraction of CO_2 from the feed, while increasing M2 and M3 areas decreases the amount of CO_2 returned to the stripping section through recycle. As shown by the corresponding response surface, the lowest residual CO_2 concentrations are obtained only when both membrane areas are sufficiently large. In contrast to the recovery requirement, the condition of less than 2 mol.% CO_2 in the residual stream is achieved only within a

comparatively narrow region of the investigated parameter space. Thus, the residual-stream specification represents a substantially more restrictive criterion for the present PSF membrane.

The influence of membrane area on product purity is qualitatively different. Increasing the enrichment-section area decreases the CO_2 concentration in the product stream. This trend was also observed in the previous studies of the cascade and is caused by the increase in stage cut in the final enrichment stage. At relatively low stage cut, the permeate is preferentially enriched in CO_2. When the membrane area is increased, the amount of CO_2 transferred continues to rise, but an increasing fraction of N_2 and O_2 also permeates through the membrane. Consequently, the total permeate flow increases faster than the selective enrichment of CO_2, leading to dilution of the final product

The same effect is visible, although less pronounced, when M1 area is increased. A larger M1 area increases the total permeate flow entering the enrichment section and promotes additional co-permeation of the less permeable components. Therefore, increasing the stripping-section area improves recovery and decreases CO_2 losses in the residual stream, but does not necessarily improve product purity. This illustrates the fundamental recovery–purity trade-off characteristic of membrane separations: increasing stage cut favors recovery, whereas lower stage cut generally favors permeate purity.

Consequently, the membrane areas in the two sections cannot be increased independently without considering the effect on all three process characteristics. The lower boundary of the acceptable operating region is determined mainly by the requirements for CO_2 recovery and, more importantly, for residual CO_2 concentration, whereas the upper practical membrane area of the enrichment section is limited by the decrease in product purity. The intersection of these restrictions defines a relatively narrow feasible operating window in which the present PSF membrane can simultaneously provide more than 80% CO_2 recovery, less than 2 mol.% CO_2 in the residual stream, and more than 70 mol.% CO_2 in the product.

The difference between these targets and the more conventional 90% recovery and 95% purity requirements is primarily associated with membrane selectivity rather than with the cascade configuration itself. Previous calculations demonstrated that the "Continuous Membrane Column" can satisfy the more stringent requirements when a membrane with sufficiently high CO_2/N_2 selectivity is used. For the binary system, the limiting selectivity was approximately 32, while for the wet four-component flue gas it increased to approximately 48. Thus, the present results should not be interpreted as an intrinsic limitation of the cascade concept, but rather as a consequence of using a technologically accessible PSF hollow-fiber membrane with moderate selectivity.

A membrane with transport characteristics close to MTR Polaris would be suitable for meeting the higher separation targets. Polaris Gen-1 has been reported with a CO_2 permeance of approximately 1000 GPU and a CO_2/N_2 selectivity of around 50, i.e., close to the selectivity identified in our previous four-component simulations as necessary for achieving high-purity CO_2 capture. However, Polaris is a proprietary thin-film composite technology rather than a generally available membrane material that can be independently fabricated or purchased as a standard polymer membrane for laboratory module production.

This distinction was one of the reasons for using PSF hollow fibers in the present study. Although their separation performance is lower than that of Polaris-type membranes, hollow fibers can be fabricated continuously using conventional phase-inversion technology, assembled into modules with high packing density, and directly integrated into the experimental cascade. The present simulation therefore serves primarily to determine a realistic operating window for the experimentally available membrane and to define membrane areas suitable for subsequent validation of the complete cascade.

3.4. Experimental CO_2 Capture and Simulation Validation

Experimental validation of the assembled Continuous Membrane Column cascade was performed by varying the operating flow rates while keeping the membrane modules, feed composition, temperature, and pressure conditions unchanged (Table 4), and the results are given in Figure 10. For comparison with the experiment, Figure 10 includes predictions from both simulation cases described above. The process-scale curves correspond to the proportionally scaled configuration used for process analysis, whereas the lab-scale curves were calculated using the actual membrane areas and the same feed-flow range as in the experiments. The overall stage cut, θ, was used as the common comparison coordinate because it characterizes the fraction of the fresh feed transferred to the CO_2-rich product side and provides a dimensionless measure of membrane utilization. The experimental data reveal a consistent change in all three performance indicators with increasing θ: the CO_2 concentration in the product decreases, the CO_2 concentration in the residual stream decreases, and CO_2 recovery increases.

Table 4. Experimental process study parameters.

Parameter	Value
Feed flow, L(N) min^{-1}	5.7–10
Pressure, MPa	0.15
Temperature, °C	51–53
Module 1	
A, m^2:	5.17
D_{outer}, mm:	63
D_{inner}, mm:	51.4
L_{active}, mm:	595
N_{fibers}:	~6450
Module 2	
A, m^2:	0.55
D_{outer}, mm:	32
D_{inner}, mm:	26.2
L_{active}, mm:	243
N_{fibers}:	~1650
Module 3	
A, m^2:	0.7
D_{outer}, mm:	32
D_{inner}, mm:	26.2
L_{active}, mm:	310
N_{fibers}:	~1650
Flue gas composition, mol.%	
N_2	73
CO_2	11.6
H_2O	11
O_2	4.4

At the lowest investigated stage cuts, the product stream contained approximately 75–76 mol.% CO_2, while the CO_2 concentration in the residual stream remained close to 2 mol.%. Increasing θ progressively intensified removal of CO_2 from the N_2-rich residual stream. In the intermediate operating region, residual CO_2 decreased to approximately 1.0–1.5 mol.%, and at the highest stage cuts it fell well below 1 mol.%. At the same time, the product purity decreased continuously. This behavior reflects the usual purity–recovery trade-off of membrane separation: increasing the fraction of gas transferred through

the membrane promotes overall capture of the preferentially permeating CO_2, but also increases co-permeation of the less permeable components, primarily N_2 and O_2, thereby diluting the CO_2-rich product.

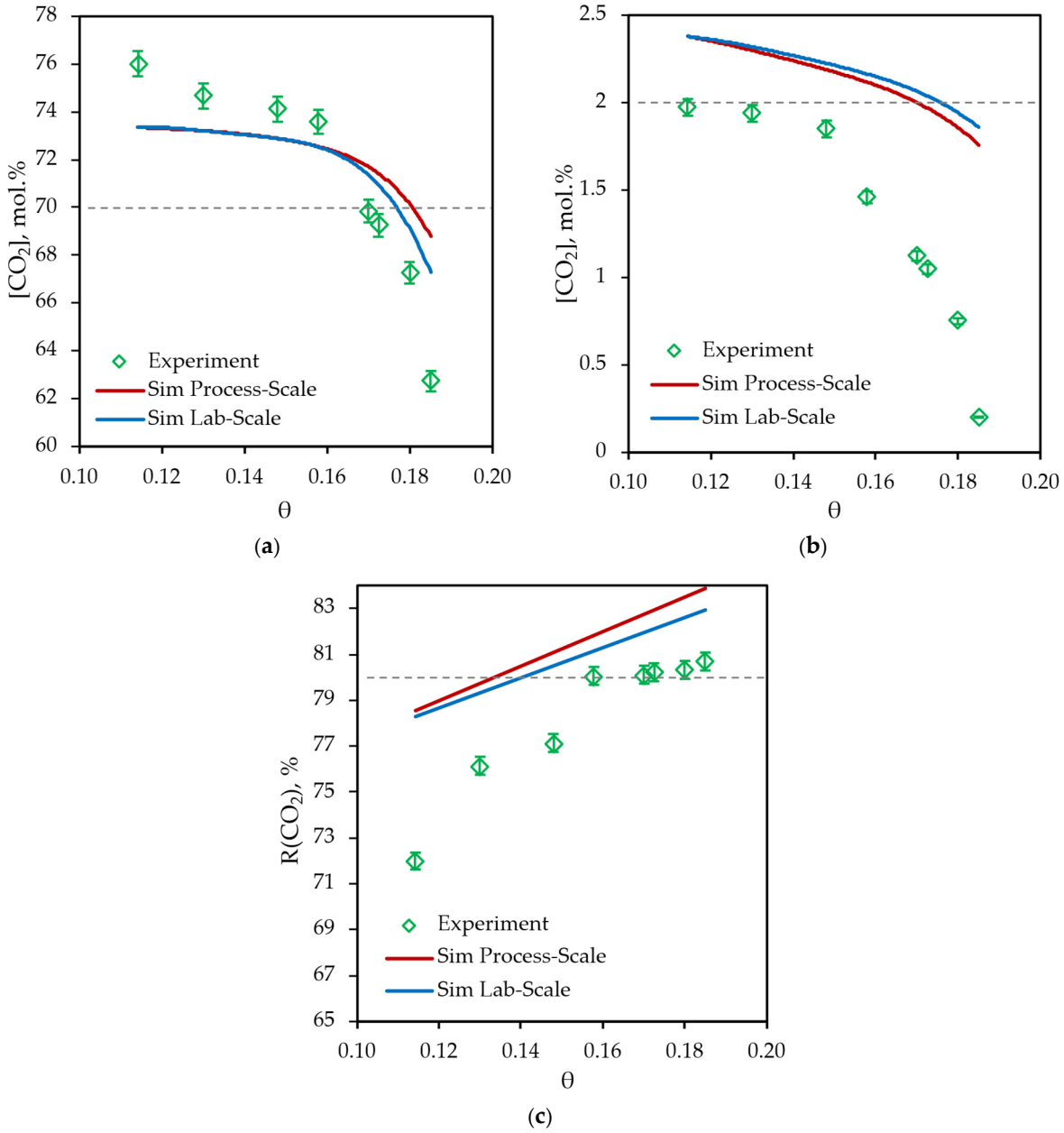


Figure 10. Experimental and simulated effects of the overall stage cut, θ, on (**a**) CO_2 concentration in the product stream, (**b**) CO_2 concentration in the residual stream, and (**c**) CO_2 recovery in the "Continuous Membrane Column" cascade. Symbols represent experimental data; the two solid curves represent the process-scale and lab-scale Aspen Plus simulations, respectively; dashed lines indicate the target process values.

The recovery data show the complementary part of the same trend. At low stage cut, the cascade operates in a high-purity but comparatively lower-recovery regime. As θ increases, a larger fraction of the incoming CO_2 is transferred to the product stream and the recovery rises from approximately 72% to more than 80%. Thus, the experimental cascade demonstrates the expected transition from a low-stage-cut regime characterized by higher product purity and lower recovery to a higher-stage-cut regime characterized by deeper CO_2 removal from the residual gas and higher recovery, but lower product purity.

Considering the target values adopted in this work—CO_2 concentration in the product above 70 mol.%, CO_2 concentration in the residual stream below 2 mol.%, and CO_2 recovery above 80%—the experimental operating window is relatively narrow. The residual-stream specification is satisfied over almost the entire investigated range and becomes increasingly easy to meet as θ increases. In contrast, the product-purity requirement limits the maximum practical stage cut, because the CO_2 concentration in the product falls below 70 mol.% at the upper part of the investigated range. The recovery requirement imposes the opposite limitation and is achieved only at sufficiently high stage cut. Consequently, the experimentally useful operating region is located near the intersection of these two opposing constraints, where the cascade provides approximately 70 mol.% or more CO_2 in the product while maintaining recovery close to or above 80% and residual CO_2 below 2 mol.%.

For a direct quantitative comparison in the practically relevant operating region, Table 5 summarizes the experimental results together with the process-scale and lab-scale simulations at overall stage cuts of approximately 0.16 and 0.17. The experimental performance metrics had a relative uncertainty of approximately 0.7–1.1%. The Aspen Plus results are deterministic calculations for the specified model inputs and are therefore reported without an experimental uncertainty. To quantify agreement, the table reports the absolute deviations between the lab-scale simulation and the corresponding experimental values.

Table 5. Quantitative comparison of experimental and simulated cascade performance in the practical operating region.

θ	CO_2	Experiment	Process-Scale Simulation	Lab-Scale Simulation	Absolute Deviation
0.16	Product, mol.%	73.58 ± 0.81	72.50	72.50	1.078
	Residual, mol.%	1.458 ± 0.02	2.12	2.16	0.702
	Recovery, %	80.05 ± 0.89	81.90	81.15	1.100
0.17	Product, mol.%	69.84 ± 0.77	71.75	71.40	1.560
	Residual, mol.%	1.123 ± 0.01	2.00	2.07	0.947
	Recovery, %	80.11 ± 0.88	82.81	81.90	1.790

The experimental results were compared with both Aspen Plus calculations using the same overall stage cut as the comparison coordinate. The process-scale and lab-scale simulations are very close over the entire investigated range and reproduce the same characteristic trends: increasing θ decreases the CO_2 concentration in both the product and residual streams while increasing CO_2 recovery. This behavior is fully consistent with the membrane-area response maps in Figure 9. In the process-scale sensitivity analysis, increasing the membrane-area-to-feed-flow ratio increases membrane utilization and stage cut, which similarly promotes deeper CO_2 removal and higher recovery at the expense of product purity. Thus, Figures 9 and 10 describe the same underlying operating trade-off using two different control variables.

The close agreement between the process-scale and lab-scale predictions shows that, within the assumptions of the present model, the principal separation behavior is governed primarily by membrane utilization, pressure ratio, membrane transport properties, and recycle topology rather than by the absolute size of the apparatus. Reducing the feed flow together with the corresponding membrane areas therefore produces only minor quantitative changes in the predicted performance. These differences are mainly associated with geometry-dependent hydrodynamic terms, particularly the axial pressure-drop profiles included in the hollow-fiber model. Consequently, the remaining discrepancy

between the lab-scale simulation and the experimental data cannot be attributed primarily to the difference in process scale.

Instead, the model–experiment deviations are more plausibly related to engineering and non-ideal effects that are not explicitly resolved by the one-dimensional constant-permeance model. In particular, the real modules contain a finite and spatially non-uniform hollow-fiber packing density, local variations in inter-fiber spacing and bundle compaction, inlet/outlet manifold effects, and possible bypass or preferential-flow regions, whereas the model represents the shell and bore sides by idealized one-dimensional flow fields. Additional sources of deviation include finite connecting volumes, fluctuations of the internal recycle flow, local pressure variations, module-to-module variability, concentration polarization, and possible composition-dependent changes in membrane permeance as the local gas composition evolves along the cascade. The laboratory-scale recalculation therefore strengthens the validation result: the model correctly captures the qualitative response of the cascade and the relevant operating window, whereas the remaining quantitative differences reflect limitations of the idealized module description rather than an artefact of comparing systems of different absolute scale.

Because the process-scale and lab-scale predictions nearly overlap, the quantitative model–experiment comparison was referenced primarily to the lab-scale simulation, which uses the actual membrane areas and experimental feed-flow range. For the CO_2-rich product, the magnitude and even the sign of the deviation depend on stage cut. At $\theta \approx 0.115$, the experimental product concentration is about 76.0 mol.% compared with approximately 73.4 mol.% predicted by the lab-scale model, i.e., an experimental value higher by about 2.6 percentage points. Near the practical operating region at $\theta \approx 0.158$, the corresponding values are approximately 73.6 and 72.5 mol.%, respectively, reducing the difference to about 1.1 percentage points. At the highest investigated stage cut, $\theta \approx 0.185$, the experimental product concentration decreases to about 62.8 mol.% while the model predicts approximately 67.3 mol.%, corresponding to a difference of about 4.5 percentage points. Thus, the largest discrepancy in product purity occurs outside the preferred operating window, where the real cascade is more sensitive to increasing stage cut than the idealized calculation.

For the residual stream, the experiment systematically shows deeper CO_2 removal than predicted. At $\theta \approx 0.115$, the measured residual CO_2 concentration is approximately 2.0 mol.% compared with about 2.38 mol.% in the lab-scale model, a difference of approximately 0.4 percentage points. Near $\theta \approx 0.158$, the measured residual concentration is about 1.46 mol.% versus approximately 2.16 mol.% predicted, so the experiment is lower by about 0.70 percentage points. At $\theta \approx 0.185$, the experimental residual CO_2 content falls to approximately 0.20 mol.%, whereas the model predicts about 1.87 mol.%, increasing the difference to approximately 1.7 percentage points. Accordingly, the experimental cascade consistently outperforms the model with respect to residual-gas CO_2 depletion, and this advantage becomes more pronounced at high membrane utilization.

The CO_2-recovery comparison shows the opposite systematic tendency: the model predicts higher recovery than measured experimentally, but the discrepancy decreases markedly in the relevant operating region. At $\theta \approx 0.115$, the experiment gives approximately 72.0% recovery compared with about 78.3% predicted by the lab-scale model, corresponding to a difference of approximately 6.3 percentage points. At $\theta \approx 0.130$–0.148, this difference decreases to approximately 3.1–3.3 percentage points. Near $\theta \approx 0.158$, where the experimental cascade reaches the adopted recovery target while retaining product purity above 70 mol.%, the experimental and predicted recoveries are approximately 80.0% and 81.1%, respectively, i.e., they differ by only about 1.1 percentage points. At the upper end of the investigated range, $\theta \approx 0.185$, the difference remains moderate: approximately 80.7% experimentally versus 82.9% predicted, or about 2.2 percentage points. These results show

that the quantitative agreement is best in the operating region of practical interest, while the larger deviations observed at non-optimal stage cuts are consistent with engineering effects and flow non-idealities that are not explicitly represented by the model.

The sensitivity analysis in Figure 11 shows that the characteristic decrease in product CO_2 concentration with increasing overall stage cut is preserved over the entire ±20% variation range of the membrane transport parameters. Proportional variation in all component permeances produces only a relatively narrow spread around the base-case curve when the results are compared at the same overall stage cut. This behavior is expected because a change in the absolute membrane permeance primarily shifts membrane utilization and, consequently, the stage cut itself, while having a smaller effect on product composition at a fixed θ.

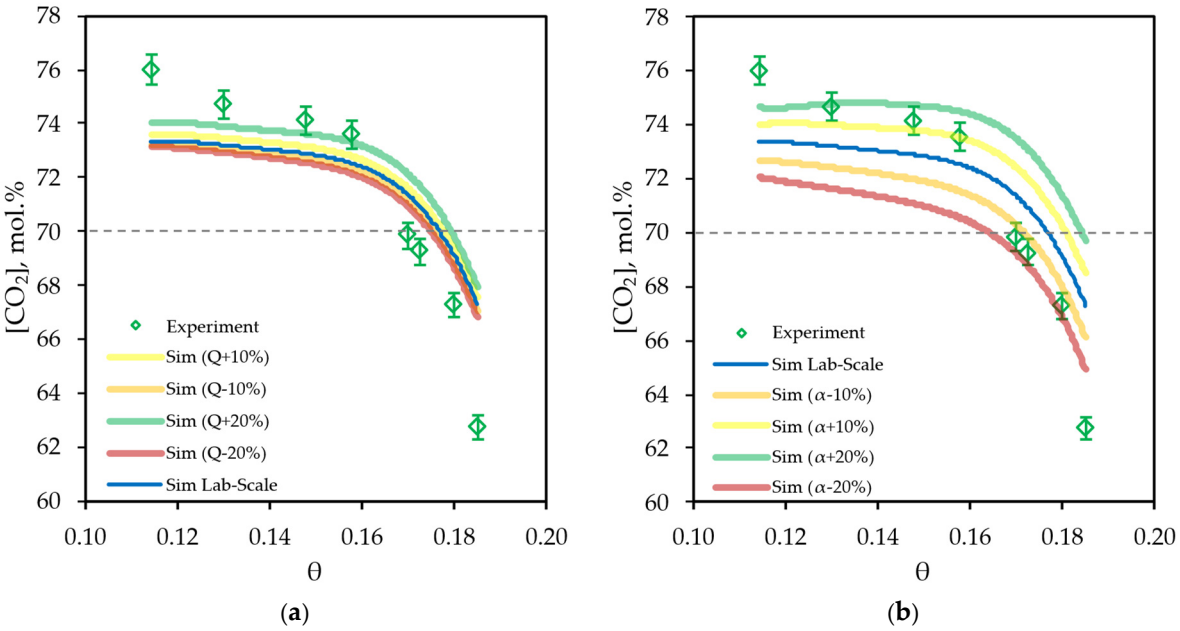


Figure 11. Sensitivity of the predicted CO_2 concentration in the product stream to variations in membrane transport properties: (**a**) proportional variation in mixed-gas permeances by ±10% and ±20%; (**b**) variation in CO_2 selectivity by ±10% and ±20%. The dark-blue curve represents the base-case lab-scale simulation.

In contrast, the predicted product composition is substantially more sensitive to changes in membrane selectivity. Variations of ±10% and ±20% in selectivity produce a progressively wider range of CO_2 product concentrations, particularly at higher stage cuts, where co-permeation of the less selective components becomes increasingly important. Nevertheless, all sensitivity cases retain the same monotonic purity–stage-cut dependence and the same general operating behavior as the base-case calculation. The experimental data in the practically relevant intermediate stage-cut region are close to the range predicted by the sensitivity calculations, whereas the larger deviations observed at the limits of the investigated range cannot be explained solely by reasonable variation in membrane transport properties. This result supports the use of experimentally measured constant mixed-gas permeances as a suitable first-order approximation for process simulation, while also confirming that the remaining model–experiment discrepancies are likely associated with module-scale hydrodynamic and engineering non-idealities.

Overall, the comparison demonstrates that the mathematical model reproduces the experimentally observed process trends and correctly identifies the trade-off between product purity, residual-stream purification, and CO_2 recovery. The remaining discrepancies are primarily quantitative rather than qualitative. The results therefore support the

use of the developed Aspen Plus model for process analysis and operating-window selection, while also indicating that further refinement of the module description—particularly with respect to composition-dependent transport and non-ideal hydrodynamics—could improve quantitative agreement with the experimental cascade.

Several limitations must therefore be considered before scale-up of the present cascade. First, pressure drop becomes increasingly important as module length, fiber number, packing density, and gas throughput increase; the resulting axial pressure loss reduces the local transmembrane driving force and may cause different sections of a large module to operate at different effective pressure ratios. Second, larger hollow-fiber bundles are more susceptible to shell-side flow maldistribution arising from non-uniform fiber packing, bundle compaction, channeling, bypass flow, and inlet/outlet manifold effects. Such effects can produce module-to-module deviations that are not captured by the present one-dimensional idealized flow description and therefore require dedicated distributor design and hydrodynamic validation at larger scale. Third, although no marked deterioration was observed during the approximately one-week experimental campaign, the present study does not establish the long-term stability of the Sylgard defect-healing treatment. Prolonged exposure to humid flue gas, repeated pressure cycling, and polymer/coating aging may alter the effectiveness of defect sealing over extended operation. A rigorous assessment of this issue would require continuous tests of at least 100–500 h, accompanied by periodic measurements of permeance, selectivity, pressure drop, and stream composition. Such long-duration operation was outside the scope of the present experimental campaign. Accordingly, future scale-up work should combine validated pressure-drop correlations and improved flow distribution with dedicated long-term stability testing of the silicone-treated hollow-fiber modules.

4. Conclusions

This work demonstrates, within a single study, the complete development pathway from membrane fabrication to process-scale validation for post-combustion CO_2 capture. Polysulfone hollow fibers were produced by dry–wet spinning, structurally and transport-characterized, defect-healed, and evaluated under both single-gas and humid four-component flue-gas conditions. The results showed that an air gap of 20 cm provided the most favorable balance between permeance and selectivity, with mixed-gas CO_2 permeance of 117 GPU and CO_2/N_2 selectivity of 21.3.

The experimentally measured multicomponent transport properties were successfully transferred into the Aspen Plus model of the three-module "Continuous Membrane Column" cascade. Process simulation showed that membrane-area distribution strongly affects CO_2 recovery, residual CO_2 concentration, and product purity, with the expected trade-off between deeper CO_2 removal and decreasing product purity at increasing membrane utilization.

Experimental testing of the complete cascade with the humid $N_2/O_2/H_2O/CO_2$ mixture confirmed the same qualitative trends predicted by the model. Increasing the overall stage cut increased CO_2 recovery and decreased CO_2 concentration in the residual stream, while reducing CO_2 concentration in the product. Within the experimentally accessible operating range, the cascade achieved approximately 80% CO_2 recovery, below 2 mol.% CO_2 in the residual stream, and about 70 mol.% CO_2 in the product.

The product purity obtained with the present PSF membrane remains limited to approximately 70 mol.% CO_2, and the practical significance of this value depends on the requirements of the downstream utilization route. If a CO_2 concentration above approximately 90–95% is required, for example for high-purity transport, storage, liquefaction, or synthesis applications, the present membrane/cascade combination cannot meet this specification without an additional purification step. This limitation is primarily associated

with the moderate CO_2/N_2 selectivity of the experimentally fabricated PSF hollow fibers rather than with the cascade configuration itself. However, a 70 mol.% CO_2 stream may already be suitable, from the standpoint of CO_2 concentration, for utilization routes that tolerate substantially lower-purity carbon dioxide, including mineral carbonation and the production of carbonate-based materials such as precipitated calcium carbonate; biological utilization routes can likewise employ CO_2-containing gas streams after controlled dilution. In such cases, the «Continuous Membrane Column» can be considered not only as a final purification unit but also as a local CO_2 capture and pre-concentration step integrated between a nearby power plant and a CO_2-consuming production facility. Such site-specific integration could avoid unnecessary deep purification when the downstream process does not require transport-grade CO_2, although the acceptability of residual impurities must be assessed for each particular application.

For industrial scale-up, the present results should therefore be regarded as a laboratory-scale validation rather than a demonstration of long-term module durability. Pressure-drop control, uniform gas distribution through larger fiber bundles, and the stability of the Sylgard defect-healing treatment during continuous 100–500 h operation remain key issues for subsequent experimental development.

Overall, the study validates the «Continuous Membrane Column» concept using independently fabricated hollow-fiber membranes and demonstrates that experimentally determined membrane properties can be used to predict the behavior of the complete separation process. The remaining deviations between simulation and experiment are mainly quantitative and indicate that further model refinement should focus on composition-dependent transport, recycle behavior, and non-ideal module hydrodynamics.

Author Contributions: Conceptualization, M.E.A. and A.N.P.; Methodology, K.A.S., V.V.Z. and S.S.S.; Validation, S.S.K.; Formal analysis, A.A.S. and A.V.V.; Investigation, M.E.A., V.V.Z. and A.N.P.; Data curation, K.A.S., S.S.K., A.A.S., S.S.S. and A.V.V.; Writing—original draft, A.A.A. and N.S.T.; Writing—review and editing, I.V.V. and N.S.T.; Supervision, A.A.A.; Project administration, I.V.V. All authors have read and agreed to the published version of the manuscript.

Funding: This work was carried out with the financial support of the Ministry of Science and Higher Education of the Russian Federation within the framework of scientific project No 075-15-2024-547.

Data Availability Statement: The original contributions presented in this study are included in the article. Further inquiries can be directed to the corresponding author.

Conflicts of Interest: The authors declare no conflicts of interest.

References

1. Gkotsis, P.; Peleka, E.; Zouboulis, A. Membrane-Based Technologies for Post-Combustion CO_2 Capture from Flue Gases: Recent Progress in Commonly Employed Membrane Materials. *Membranes* **2023**, *13*, 898. https://doi.org/10.3390/MEMBRANES13120898.
2. Favre, E. Membrane Separation Processes and Post-Combustion Carbon Capture: State of the Art and Prospects. *Membranes* **2022**, *12*, 884. https://doi.org/10.3390/MEMBRANES12090884.
3. Hou, R.; Fong, C.; Freeman, B.D.; Hill, M.R.; Xie, Z. Current Status and Advances in Membrane Technology for Carbon Capture. *Sep. Purif. Technol.* **2022**, *300*, 121863. https://doi.org/10.1016/J.SEPPUR.2022.121863.
4. Dai, Z.; Deng, L. Membranes for CO_2 Capture and Separation: Progress in Research and Development for Industrial Applications. *Sep. Purif. Technol.* **2024**, *335*, 126022. https://doi.org/10.1016/J.SEPPUR.2023.126022.
5. Fu, J.; Ahmad, N.N.R.; Leo, C.P.; Aberilla, J.M.; Dela Cruz, I.J.; Alamani, B.; Koh, S.P. Techno-Economic and Life Cycle Assessment of Membrane Separation in Post-Combustion Carbon Capture: A Review. *Gas Sci. Eng.* **2024**, *129*, 205401. https://doi.org/10.1016/J.JGSCE.2024.205401.
6. Liu, M.; Nothling, M.D.; Zhang, S.; Fu, Q.; Qiao, G.G. Thin Film Composite Membranes for Postcombustion Carbon Capture: Polymers and Beyond. *Prog. Polym. Sci.* **2022**, *126*, 101504. https://doi.org/10.1016/J.PROGPOLYMSCI.2022.101504.

7. Wu, J.; Hillman, F.; Liang, C.Z.; Jia, Y.; Zhang, S. Progressing Thin-Film Membrane Designs for Post-Combustion CO_2 Capture: Performance or Practicality? *J. Mater. Chem. A Mater.* **2023**, *11*, 17452–17478. https://doi.org/10.1039/D3TA02842A.
8. Yu, M.C.; Bai, L.J.; Moioli, S.; Tontiwachwuthikul, P.; Plisko, T.V.; Bildyukevich, A.V.; Feng, Y.N.; Liu, H. Hybrid CO_2 Capture Processes Consisting of Membranes: A Technical and Techno-Economic Review. *Adv. Membr.* **2023**, *3*, 100071. https://doi.org/10.1016/J.ADVMEM.2023.100071.
9. Khalilpour, R.; Mumford, K.; Zhai, H.; Abbas, A.; Stevens, G.; Rubin, E.S. Membrane-Based Carbon Capture from Flue Gas: A Review. *J. Clean. Prod.* **2015**, *103*, 286–300. https://doi.org/10.1016/J.JCLEPRO.2014.10.050.
10. Scholes, C.A.; Ho, M.T.; Wiley, D.E.; Stevens, G.W.; Kentish, S.E. Cost Competitive Membrane-Cryogenic Post-Combustion Carbon Capture. *Int. J. Greenh. Gas Control* **2013**, *17*, 341–348. https://doi.org/10.1016/j.ijggc.2013.05.017.
11. Han, Y.; Ho, W.S.W. Polymeric Membranes for CO_2 Separation and Capture. *J. Memb. Sci.* **2021**, *628*, 119244. https://doi.org/10.1016/J.MEMSCI.2021.119244.
12. Hu, L.; Clark, K.; Alebrahim, T.; Lin, H. Mixed Matrix Membranes for Post-Combustion Carbon Capture: From Materials Design to Membrane Engineering. *J. Memb. Sci.* **2022**, *644*, 120140. https://doi.org/10.1016/J.MEMSCI.2021.120140.
13. Sandru, M.; Prache, M.; Macron, T.; Căta, L.; Ahunbay, M.G.; Hägg, M.B.; Maurin, G.; Barboiu, M. Rubbery Organic Frameworks (ROFs) toward Ultrapermeable CO_2-Selective Membranes. *Sci. Adv.* **2024**, *10*, eadq5024. https://doi.org/10.1126/SCIADV.ADQ5024.
14. Huang, Y.; Merkel, T.C.; Baker, R.W. Pressure Ratio and Its Impact on Membrane Gas Separation Processes. *J. Memb. Sci.* **2014**, *463*, 33–40. https://doi.org/10.1016/J.MEMSCI.2014.03.016.
15. Roussanaly, S.; Anantharaman, R.; Lindqvist, K.; Zhai, H.; Rubin, E. Membrane Properties Required for Post-Combustion CO_2 Capture at Coal-Fired Power Plants. *J. Memb. Sci.* **2016**, *511*, 250–264. https://doi.org/10.1016/J.MEMSCI.2016.03.035.
16. Giordano, L.; Roizard, D.; Bounaceur, R.; Favre, E. Evaluating the Effects of CO_2 Capture Benchmarks on Efficiency and Costs of Membrane Systems for Post-Combustion Capture: A Parametric Simulation Study. *Int. J. Greenh. Gas Control* **2017**, *63*, 449–461. https://doi.org/10.1016/J.IJGGC.2017.05.002.
17. Zhao, L.; Riensche, E.; Blum, L.; Stolten, D. Multi-Stage Gas Separation Membrane Processes Used in Post-Combustion Capture: Energetic and Economic Analyses. *J. Memb. Sci.* **2010**, *359*, 160–172. https://doi.org/10.1016/j.memsci.2010.02.003.
18. Ramasubramanian, K.; Verweij, H.; Winston Ho, W.S. Membrane Processes for Carbon Capture from Coal-Fired Power Plant Flue Gas: A Modeling and Cost Study. *J. Memb. Sci.* **2012**, *421–422*, 299–310. https://doi.org/10.1016/J.MEMSCI.2012.07.029.
19. Mat, N.C.; Lipscomb, G.G. Membrane Process Optimization for Carbon Capture. *Int. J. Greenh. Gas Control* **2017**, *62*, 1–12. https://doi.org/10.1016/j.ijggc.2017.04.002.
20. Brinkmann, T.; Pohlmann, J.; Bram, M.; Zhao, L.; Tota, A.; Jordan Escalona, N.; de Graaff, M.; Stolten, D. Investigating the Influence of the Pressure Distribution in a Membrane Module on the Cascaded Membrane System for Post-Combustion Capture. *Int. J. Greenh. Gas Control* **2015**, *39*, 194–204. https://doi.org/10.1016/J.IJGGC.2015.03.010.
21. Watson, J.C.; Pennisi, K.J.; Parrish, C.; Majumdar, S. Techno-Economic Process Optimization for a Range of Membrane Performances: What Provides Real Value for Point-Source Carbon Capture? *Carbon Capture Sci. Technol.* **2024**, *11*, 100182. https://doi.org/10.1016/J.CCST.2023.100182.
22. Adhikari, B.; Orme, C.J.; Stetson, C.; Klaehn, J.R. Techno-Economic Analysis of Carbon Dioxide Capture from Low Concentration Sources Using Membranes. *Chem. Eng. J.* **2023**, *474*, 145876. https://doi.org/10.1016/J.CEJ.2023.145876.
23. Merkel, T.C.; Lin, H.; Wei, X.; Baker, R. Power Plant Post-Combustion Carbon Dioxide Capture: An Opportunity for Membranes. *J. Memb. Sci.* **2010**, *359*, 126–139. https://doi.org/10.1016/J.MEMSCI.2009.10.041.
24. White, L.S.; Wei, X.; Pande, S.; Wu, T.; Merkel, T.C. Extended Flue Gas Trials with a Membrane-Based Pilot Plant at a One-Ton-per-Day Carbon Capture Rate. *J. Memb. Sci.* **2015**, *496*, 48–57. https://doi.org/10.1016/J.MEMSCI.2015.08.003.
25. White, L.S.; Amo, K.D.; Wu, T.; Merkel, T.C. Extended Field Trials of Polaris Sweep Modules for Carbon Capture. *J. Memb. Sci.* **2017**, *542*, 217–225. https://doi.org/10.1016/j.memsci.2017.08.017.
26. Pohlmann, J.; Bram, M.; Wilkner, K.; Brinkmann, T. Pilot Scale Separation of CO_2 from Power Plant Flue Gases by Membrane Technology. *Int. J. Greenh. Gas Control* **2016**, *53*, 56–64. https://doi.org/10.1016/j.ijggc.2016.07.033.
27. He, X.; Lindbråthen, A.; Kim, T.J.; Hägg, M.B. Pilot Testing on Fixed-Site-Carrier Membranes for CO_2 Capture from Flue Gas. *Int. J. Greenh. Gas Control* **2017**, *64*, 323–332. https://doi.org/10.1016/J.IJGGC.2017.08.007.
28. Wu, H.; Li, Q.; Guo, B.; Sheng, M.; Wang, D.; Mao, S.; Ye, N.; Qiao, Z.; Kang, G.; Cao, Y.; et al. Industrial-Scale Spiral-Wound Facilitated Transport Membrane Modules for Post-Combustion CO_2 Capture: Development, Investigation and Optimization. *J. Memb. Sci.* **2023**, *670*, 121368. https://doi.org/10.1016/J.MEMSCI.2023.121368.

29. Micari, M.; Dakhchoune, M.; Agrawal, K.V. Techno-Economic Assessment of Postcombustion Carbon Capture Using High-Performance Nanoporous Single-Layer Graphene Membranes. *J. Memb. Sci.* **2021**, *624*, 119103. https://doi.org/10.1016/J.MEMSCI.2021.119103.
30. Bounaceur, R.; Berger, E.; Pfister, M.; Ramirez Santos, A.A.; Favre, E. Rigorous Variable Permeability Modelling and Process Simulation for the Design of Polymeric Membrane Gas Separation Units: MEMSIC Simulation Tool. *J. Memb. Sci.* **2017**, *523*, 77–91. https://doi.org/10.1016/J.MEMSCI.2016.09.011.
31. Lim, Y.G.; Bak, C. u.; Kim, Y.D. Comprehensive Experimental and Theoretical Insights into the Performance of Polysulfone Hollow-Fiber Membrane Modules in Biogas Purification Process. *Chem. Eng. J.* **2022**, *433*, 134616. https://doi.org/10.1016/J.CEJ.2022.134616.
32. Jasrotia, S.; Puttaiahgowda, Y.M.; Praveen, B.M. Polysulfone-Based Membranes for Industrial CO_2 Capture: Advanced Fabrication Strategies, Performance Enhancement, and Commercial Viability—A Review. *Process Saf. Environ. Prot.* **2025**, *203*, 107964. https://doi.org/10.1016/J.PSEP.2025.107964.
33. Atlaskin, A.A.; Trubyanov, M.M.; Yanbikov, N.R.; Bukovsky, M.V.; Drozdov, P.N.; Vorotyntsev, V.M.; Vorotyntsev, I.V. Total Reflux Operating Mode of Apparatuses of a Membrane Column Type during High Purification of Gases to Remove a Highly Permeable Impurity. *Pet. Chem.* **2018**, *58*, 508–517. https://doi.org/10.1134/S0965544118060026.
34. Atlaskin, A.A.; Petukhov, A.N.; Stepakova, A.N.; Tsivkovsky, N.S.; Kryuchkov, S.S.; Smorodin, K.A.; Moiseenko, I.S.; Atlaskina, M.E.; Suvorov, S.S.; Stepanova, E.A.; et al. Membrane Cascade Type of «Continuous Membrane Column» for Power Plant Post-Combustion Carbon Dioxide Capture Part 1: Simulation of the Binary Gas Mixture Separation. *Membranes* **2023**, *13*, 270. https://doi.org/10.3390/MEMBRANES13030270.
35. Smorodin, K.A.; Atlaskin, A.A.; Kryuchkov, S.S.; Atlaskina, M.E.; Tsivkovsky, N.S.; Sysoev, A.A.; Zhmakin, V.V.; Petukhov, A.N.; Suvorov, S.S.; Vorotyntsev, A.V.; et al. Comparative Simulation and Optimization of "Continuous Membrane Column" Cascades for Post-Combustion CO_2 Capture. *Energies* **2026**, *19*, 303. https://doi.org/10.3390/EN19020303.
36. Otvagina, K.V.; Atlaskin, A.A.; Trubyanov, M.M.; Kryuchkov, S.S.; Smorodin, K.A.; Mochalova, A.E.; Vorotyntsev, I.V. Effect of Moisture Presence on Gas Permeability through Gas Separation Membranes Based on Poly(Vinyltrimethylsilane) and Quaternized Chitosan. *Membr. Membr. Technol.* **2020**, *2*, 125–131. https://doi.org/10.1134/S2517751620020092.
37. Pinnau, I.; Koros, W.J. Structures and Gas Separation Properties of Asymmetric Polysulfone Membranes Made by Dry, Wet, and Dry/Wet Phase Inversion. *J. Appl. Polym. Sci.* **1991**, *43*, 1491–1502. https://doi.org/10.1002/APP.1991.070430811.
38. Kluge, S.; Kose, T.; Tutuş, M. Tuning the Morphology and Gas Separation Properties of Polysulfone Membranes. *Membranes* **2022**, *12*, 654. https://doi.org/10.3390/MEMBRANES12070654.
39. Pesek, S.C.; Koros, W.J. Aqueous Quenched Asymmetric Polysulfone Membranes Prepared by Dry/Wet Phase Separation. *J. Memb. Sci.* **1993**, *81*, 71–88. https://doi.org/10.1016/0376-7388(93)85032-R.
40. Pesek, S.C.; Koros, W.J. Aqueous Quenched Asymmetric Polysulfone Hollow Fibers Prepared by Dry/Wet Phase Separation. *J. Memb. Sci.* **1994**, *88*, 1–19. https://doi.org/10.1016/0376-7388(93)E0150-I.
41. Pinnau, I.; Koros, W.J. Influence of Quench Medium on the Structures and Gas Permeation Properties of Polysulfone Membranes Made by Wet and Dry/Wet Phase Inversion. *J. Memb. Sci.* **1992**, *71*, 81–96. https://doi.org/10.1016/0376-7388(92)85008-7.
42. Metz, S.J.; Van De Ven, W.J.C.; Potreck, J.; Mulder, M.H.V.; Wessling, M. Transport of Water Vapor and Inert Gas Mixtures through Highly Selective and Highly Permeable Polymer Membranes. *J. Memb. Sci.* **2005**, *251*, 29–41. https://doi.org/10.1016/j.memsci.2004.08.036.
43. Țiuleanu, P.; Atlaskin, A.A.; Smorodin, K.A.; Kryuchkov, S.S.; Atlaskina, M.E.; Petukhov, A.N.; Vorotyntsev, A.V.; Tsivkovskiy, N.S.; Sysoev, A.A.; Vorotyntsev, I.V. The Production of High-Permeable and Macrovoid-Free Polysulfone Hollow Fiber Membranes and Their Utilization in CO_2 Capture Applications via the Membrane-Assisted Gas Absorption Technique. *Polymers* **2025**, *17*, 1407. https://doi.org/10.3390/POLYM17101407.
44. Chou, C.H.; Huang, Y.H.; Hwang, J.J.J.; Tseng, H.H.; Wang, M.J.; Chung, T.S. Tri-Bore Composite Hollow Fiber Membranes Consisting of Nano CQDs and PolyActive™ for CO_2 Capture. *J. Memb. Sci.* **2025**, *730*, 124196. https://doi.org/10.1016/J.MEMSCI.2025.124196.
45. Chen, D.; Li, L.; Semiat, R.; He, X. Process Parametric Investigation of Graphene-Oxide-Embedded Composite Membranes for Boosting CO_2/N_2 Separation. *Energy Fuels* **2023**, *37*, 11187–11196. https://doi.org/10.1021/ACS.ENERGYFUELS.3C01927.

Disclaimer/Publisher's Note: The statements, opinions and data contained in all publications are solely those of the individual author(s) and contributor(s) and not of MDPI and/or the editor(s). MDPI and/or the editor(s) disclaim responsibility for any injury to people or property resulting from any ideas, methods, instructions or products referred to in the content.